Halide Containing Short Organic Monocations in n = 1–4 2D Multilayered Halide Perovskite Thin Films and Crystals

Alla Skorokhod, Claudio Quarti, Alexandre Abhervé, Magali Allain, Jacky Even, Claudine Katan, Nicolas Mercier

To cite this version:

Alla Skorokhod, Claudio Quarti, Alexandre Abhervé, Magali Allain, Jacky Even, et al.. Halide Containing Short Organic Monocations in n = 1–4 2D Multilayered Halide Perovskite Thin Films and Crystals. Chemistry of Materials, 2023, 35 (7), pp.2873-2883. 10.1021/acs.chemmater.2c03718 . hal-04064243

HAL Id: hal-04064243
https://hal.science/hal-04064243

Submitted on 11 Apr 2023

1Halide containing short organic monocations in n=1-4 2D multilayered halide perovskite thin films and crystals

Alla Skorokhod,[a] Claudio Quarti,*[,b-c] Alexandre Abhervé, [a] Magali Allain,[a] Jacky Even,[d]
Claudine Katan,[b] Nicolas Mercier*[,a]

[a] MOLTECH ANJOU, UMR-CNRS 6200, Université d'Angers, 2 Bd Lavoisier, 49045 Angers, France

[b] Univ Rennes, ENSCR, INSA Rennes, CNRS, ISCR (Institut des Sciences Chimiques de Rennes) – UMR 6226, F-35000 Rennes, France

[c] Laboratory for Chemistry of Novel Materials, Materials Research Institute, University of Mons, Place du Parc 20, 7000-Mons, Belgium

[d] Univ Rennes, INSA Rennes, CNRS, Institut FOTON - UMR 6082, F-35000 Rennes, France

Corresponding authors: claudio.quarti@umons.ac.be

nicolas.mercier@univ-angers.fr

Abstract

Low electronic band gap 2D multilayered (n=3,4) lead-iodide perovskites with formula $A'_2A_{n-1}Pb_nI_{3n+1}$ and $A''A_{n-1}Pb_nI_{3n+1}$ are of great interest for photovoltaics, with recent demonstrations of stable solar cell operation based on 2D/3D bilayered heterostructures. Still, the difficulty in achieving optimal phase control, with potential formation of mixed n-domains, is a limiting factor for photovoltaic performance of 2D/3D heterostructures, and the current choice for multi n- layered compounds is limited. Here we report synthesis and XRD characterization of novel $(I\text{-}EA)_2MA_{n-1}Pb_nI_{3n+1}$ (n=1-4) compound series, along with $(Br\text{-}EA)_2PbBr_4$ (n=1) compound, incorporating iodo-ethylammonium (I-EA) and bromo-ethylammonium (Br-EA) spacers. These halide-featuring spacers lead to small lattice mismatch between the inorganic and organic components, that explains the successful formation of multi n- layered compounds. The presence of bromine or iodine in the interlayer space impacts on the dielectric and electronic properties of these materials. Periodic DFT simulations predict vertical hole effective mass for n=1 $(I\text{-}EA)_2PbI_4$ as small as 1.8 m_e, comparable to popular organic semiconductors, like rubrene. UV-vis characterization sets the optical absorption onset of these materials around 1.71 eV for n=3 and 4, hence suggesting these compounds can be successfully implemented in 2D/3D photovoltaic architectures.

Introduction

Two-Dimensional (2D) lead-iodide perovskites are swiftly emerging as promising semiconductors for opto-electronics applications.[1–9] These inorganic/organic hybrids derive from the archetypal 3D $APbI_3$ perovskite structure (A= methylammonium, formamidinium, Cs) by intercalating atomically-thin lead-iodide perovskite sheets with bulky organic cations A' or dications A", acting as spacers. Resulting materials have formula $A'_2A_{n-1}Pb_nI_{3n+1}$ or $A''A_{n-1}Pb_nI_{3n+1}$, with "n" indicating the number of PbI_6 octahedra stacked along the thickness of the individual perovskite sheet. With most common alkyl- or small aromatic-based spacers, layered perovskites correspond to natural quantum wells, the photogenerated carriers being constrained within the inorganic frame by quantum and dielectric confinement.[10] Thanks to the combination of the excellent semiconducting properties of the lead-iodide perovskite network with the chemical stability against moisture of the hydrophobic organic spacer, these hybrids and related nanostructures are more and more studied for applications in light-emission,[1–4] sensing,[5,6] and energy conversion,[7–9] paving the way for performant and durable devices. More, multilayered (n=3,4) 2D perovskites combined with 3D halide perovskites in bilayer structures lead to state of the art solar cell efficiencies, while inheriting their stability from the 2D layer.[11,12] Multilayered (n=3,4) 2D compounds are also necessary to achieve matching of the valence band levels with those of the 3D perovskites in these heterostructures.[11] Therefore, new $A'_2A_{n-1}Pb_nI_{3n+1}$ or $A''A_{n-1}Pb_nI_{3n+1}$ compounds with n=3,4 thickness are of huge interest for photovoltaics, as their exploitation in 2D/3D heterostructures is one of the most promising routes for decisive progresses toward the industrialization and commercialization of halide perovskite photovoltaic technology.[11,12]

Successful synthesis of thick (n>2) layered lead halide perovskites, as well as control over phase purity, is however not an easy task and only few examples of phase-controlled, multilayered 2D lead iodide compounds have been reported and fully characterized in the literature, thus far. Most notable examples are represented by $(PEA)_2(MA)_{n-1}Pb_nI_{3n+1}$ (n=2-3) (PEA=phenylethylammonium, MA=methylammonium),[13,14] $(BA)_2(MA)_{n-1}Pb_nI_{3n+1}$ (n=2-7) (BA=butylammonium),[15,16] $(3\text{-}4AMPY)(MA)_{n-1}Pb_nI_{3n+1}$ (n=1-4) (3-4AMPY=aminoethylpyridinium),[17] and $(3\text{-}4AMP)(MA)_{n-1}Pb_nI_{3n+1}$ (n=1-4) (3-4AMP=aminoethylpiperidinium),[18] the latter recently demonstrating champion photovoltaic efficiency of 18.3%, for 2D-perovskite based devices.[9] In addition to phase purity issues, another factor limiting the photovoltaic efficiency of 2D-perovskite based devices compared to 3D-based ones (25.7%)[19] is the ineffective charge and energy transport perpendicular to the inorganic sheet. The interplanar transport bottleneck was shown by Tsai *et al.*, via selectively growth of 2D perovskite thin films with inorganic sheets orienting perpendicularly to the selective contacts, hence creating a continuous percolation path for charge carrier extraction within the perovskite frame. This led to an efficiency increase up to 12.5%,[12] compared to 4.7% of traditional design with perovskite sheets lying parallel to the contacts.[20] Further exploitation of 2D layered perovskite compounds therefore may benefit from the design of new compounds with both ease phase purity control and improved out-of-plane transport, with two main strategies currently exploited to cure the latter issue. The first consists in decreasing the distance between adjacent perovskite planes, hence reducing the spatial extension of the potential barrier due to the presence of the spacer. This strategy requires small size organic spacers, and was demonstrated by Mao *et al.*,[18] and Li *et al.*, [17] via incorporation of 3-4AMP, and 3-4AMPY spacers, respectively (interlayer distance ~ 4.12 Å) and by Nazarenko *et al.*,[21] exploting mixed Guanidinium/Cs spacers (~ 4.4 Å). The other strategy consists in dropping the traditional concept of organic spacer as a barrier to carrier transport,[10] and to exploit electronically active π-conjugated organic spacers. This strategy was pioneered by Mitzi et al.,[22] and more recently by Gao et al.,[23] with incorporation of quaterthiophene derivatives leading to the formation of type II structure at the organic/inorganic interface (the HOMO or LUMO of the organic spacer embedded in the inorganic band gap). Similar findings were reported recently by Lédée *et al.*, by exploiting much smaller tetrazine-based moiety as organic spacer, further demonstrating the flexibility of the organic part.[24]

In 2007, Sourisseau *et al.* synthesized pure phase, n=1 layered halide perovskite materials incorporating halide containing $X\text{-}(CH_2)_2\text{-}NH_3^+$ (X=Cl, Br, I) organic spacer, with successful formation of layered perovskite structures verified via single crystal XRD measurements.[25] In addition to the demonstration of the indirect effect of the organic component on the optical properties of the inorganic, via spacer-driven structural distortion, this work demonstrated the feasibility of introducing heavy halides (Br or I) also in the organic component. More recently, Chakraborty *et al.* reported a series of n=1 $(I\text{-}(CH_2)_m\text{-}NH_3)_2PbI_4$ (m=2-6) layered perovskites, showing the impact of iodine-iodine contacts on phase transitions of materials.[26] Smith *et al.* also demonstrated the role of the halide in the interlayer space in tuning the optical properties of these hybrids. In particular, the intercalation of I_2 molecules was shown to lead to inversion of the dielectric contrast between the well and the barrier (larger dielectric constant in the barrier than in the inorganic layer), as well as structural distorsions.[27]

Inspired by this design concept, we report here the synthesis of a novel $(I\text{-}EA)_2MA_{n-1}Pb_nI_{3n+1}$ 2D halide perovskite series, featuring halide containing iodoethylammonium (I-EA) as spacer. Phase control for thickness going from n=1,2 to technologically relevant n=3,4[11] is demonstrated via low temperature XRD characterization. We also report fully brominated n=1 $(Br\text{-}EA)_2PbBr_4$ (Br-EA=bromoethylammonium) compound, demonstrating the flexibility in the choice of the halide. UV-vis measurements indicate optical band gaps from 2.38 eV to 1.71 eV, for n=1 and n=4 compounds, respectively, hence falling in similar range than champion efficiency $(4AMP)MA_2Pb_3I_{10}$ layered perovskite.[18] Electronic structure calculations confirm the formation of type I heterostructures but also highlight the direct role from the I-EA spacer in improving the vertical transport. DFT-calculated effective masses for holes reach values down to 1.8 m_e, comparable to promising organic molecular semiconductors, like rubrene or BTBT.[28–30]

Methods

Material synthesis. All reagents were used as received from Sigma Aldrich without further purification: 2-Bromoethylamine hydrobromide ($Br\text{-}C_2H_4\text{-}NH_2$•HBr 99%), methylamine hydroiodide (CH_3NH_2•HI, 99%), Lead(II) iodide (PbI_2 99%), hydriodic acid (HI, 57 wt% in H_2O, stabilized). The reagents ($Br\text{-}C_2H_4\text{-}NH_2$•HBr, CH_3NH_2•HI, PbI_2 -see details for each experiment leading to n= 1-4 in Table S1) were dissolved in 57% w/w aqueous HI solution in a 50 mL glass flacon by heating to boiling (150°C, hot plate) under constant magnetic stirring for about 10 min (flask closed with a cap), to substitute Br for I in bromoethylammonium cation to give iodoethylammonium cations $I\text{-}EA^+$. The stirring was then interrupted and the heating was turned off. The solution was left to cool down to room temperature. Plate-like crystals were slowly precipitated: yellow for n=1, red for n=2 and black for n=3-4. The crystals were isolated by suction filtration and thoroughly dried under reduced pressure. Powder X-Ray diffraction (PXRD) analysis which was measured on a D8 Bruker diffractometer (Cu Kα, λ=1.5418 Å) equipped with a linear Vantec super speed detector, confirmed the phase purity of the four n=1,4 $(I\text{-}EA)_2MA_{n-1}Pb_nI_{3n+1}$ compounds (Figure S1-S4) and for the $(Br\text{-}EA)_2PbBr_4$ compound (Figure S5). Moreover, solution ^1H NMR spectroscopy of materials dissolved in deuterated DMSO well confirms the expected X-EA/MA ratio (X=Br, I) of 2, 1 and 0.67 for the n= 2, n= 3 and n= 4 compounds, respectively (Figure S6).

Thin films preparation) All solutions preparation and thin films processing steps were carried out in ambient conditions. The Pre-patterned Glass FTO substrates were purchased from Pilkington. They were sequentially cleaned in 2.5M NaOH ethanol solution, water and acetone, then dried at 450 °C overnight. Precursor solutions were prepared by dissolving PbI_2, methylamine iodide (MAI), and $(I\text{-}EA)_2PbI_4$ (n=1, previously synthesized) in anhydrous DMSO, in accordance with the expected stoichiometry for n=1-4 compounds (details in Table S2). Before spin-coating, solutions and substrates were heated for 1 minute at 150°C. Centrifugation was applied during 20 seconds at 5000 rotations per minute (rpm). After centrifugation, the films were placed on a hot plate at 150°C for 5 minutes.

UV-vis characterization. The UV-visible absorption spectra of crystallized powders and thin films were measured with a PerkinElmer LAMBDA 950 spectrophotometer with integration sphere, at room conditions, resolution of 2 nm.

Table 1. Structural details for the investigated perovskite $(I\text{-}EA)_2MA_{n-1}Pb_nI_{3n+1}$ compounds (n=1-4) and for the n=1 $(Br\text{-}EA)_2PbBr_4$ compound. (RT=Room Temperature)

	n=1	**n=2**	**n=2**	**n=3**	**n=4**	**BrEA**
	120 K	**RT**	**150 K**	**150 K**	**150 K**	**150 K**
Fw (g/mol)	1058.77	1678.72	1678.2	2298.71	2916.63	776.77
space group	$P2_1/c$	P-1	P-1	$P2_1/c$	P-1	P-1
a, Å	12.5049(4)	8.8172(8)	8.8125(4)	25.189(1)	8.7713(3)	8.2313(4)
b, Å	8.7414(3)	8.9178(4)	17.410(1)	8.8768(5)	8.8359(3)	13.6632(6)
c, Å	8.6297(3)	19.213(2)	19.632(1)	8.6144(5)	31.422(1)	15.8766(6)
α, °	90	82.67(1)	107.56(1)	90	85.631(3)	66.190(4)
β, °	97.88(1)	83.40(1)	96.00(1)	94.35(1)	85.116(3)	81.310(4)
γ, °	90	90.07(1)	90.36(4)	90	89.997(3)	80.955(4)
V, Å^3	934.41(5)	1488.3(2)	2855.3(3)	1916.8(2)	2419.4(1)	1605.7(1)
Z	2	2	4	2	2	4
obs. reflns $(I>2\sigma(I))$ /R_{int}	1756 /0.029	3134 /0.106	6491 /0.058	3388 /0.056	7261 / 0.032	5394 / 0.057
parameters	62	175	345			
$R1(I>2\sigma(I))$ /wR2(all data)	0.048 / 0.125	0.091 / 0.239	0.070 /0.201	0.078 / 0.215	0.062 / 0.169	0.060 / 0.174

Single crystal XRD characterization. X-ray diffraction data were collected at T = 120 K (n =1), 150 K (n= 2-4) and 293 K for n= 2 on an Agilent SuperNova diffractometer equipped with Atlas CCD detector and micro-focus Cu-Kα radiation (λ = 1.54184 Å). Intensities were corrected for Lorentz-polarization effects, as well as for absorption effect (multi-scan method using CrysAlisPro program -CrysAlisPro, Agilent Technologies, V1.171.38.46, 2015). The structures were solved using SHELXT program, and refined by full matrix least-squares routines against F2 using SHELXT programs. The hydrogen atoms were treated with a riding model. A summary of crystallographic data and refinement results is provided in Table 1, while more complete data appear in Tables S3-S7 for $(I\text{-}EA)_2MA_{n-1}Pb_nI_{3n+1}$ compounds and in Table S8 for $(Br\text{-}EA)_2PbI_4$. A complete list of crystallographic data, along with the atomic coordinates, the anisotropic displacement parameters and bond distances and angles for each compound, are given as CIF file. CCDC numbers 2223697 (n= 1); 2223698 and 2223699 (n= 2 RT and 150 K); 2223700 (n= 3); 2223702 (n= 4) and 2223701 ($(BrEA)_2PbBr_4$).

Electronic structure simulations. Crystalline models from XRD are used as input for periodic Density Functional Theory (DFT) simulations. Band structures are calculated within the pseudopotential/plane-waves formalism, as implemented in the Quantum-Espresso suite program.[31] The diagonal components of the hole/electron effective mass tensor are then computed from numerical fit of the curvature of the top valence/bottom conduction band along the indirect lattice directions associated either to the inorganic plane (for in-plane effective masses) or to the plane stacking direction. High-frequency dielectric profiles are instead calculated using the SIESTA package,[32] following the approach proposed in Ref.[33]. This consists in estimating the induced polarization in presence of external electric fields. Here, the exciton states are modelled using the 3D momentum space representation of the BSE for the polarization function and assuming an effective mass approximation for the electronic dispersions of the edge states close to the band gap.[34] Detailed description of all computational procedures and related references are reported in the Supporting Information, including sampling of the Brillouin zone (Table S9).

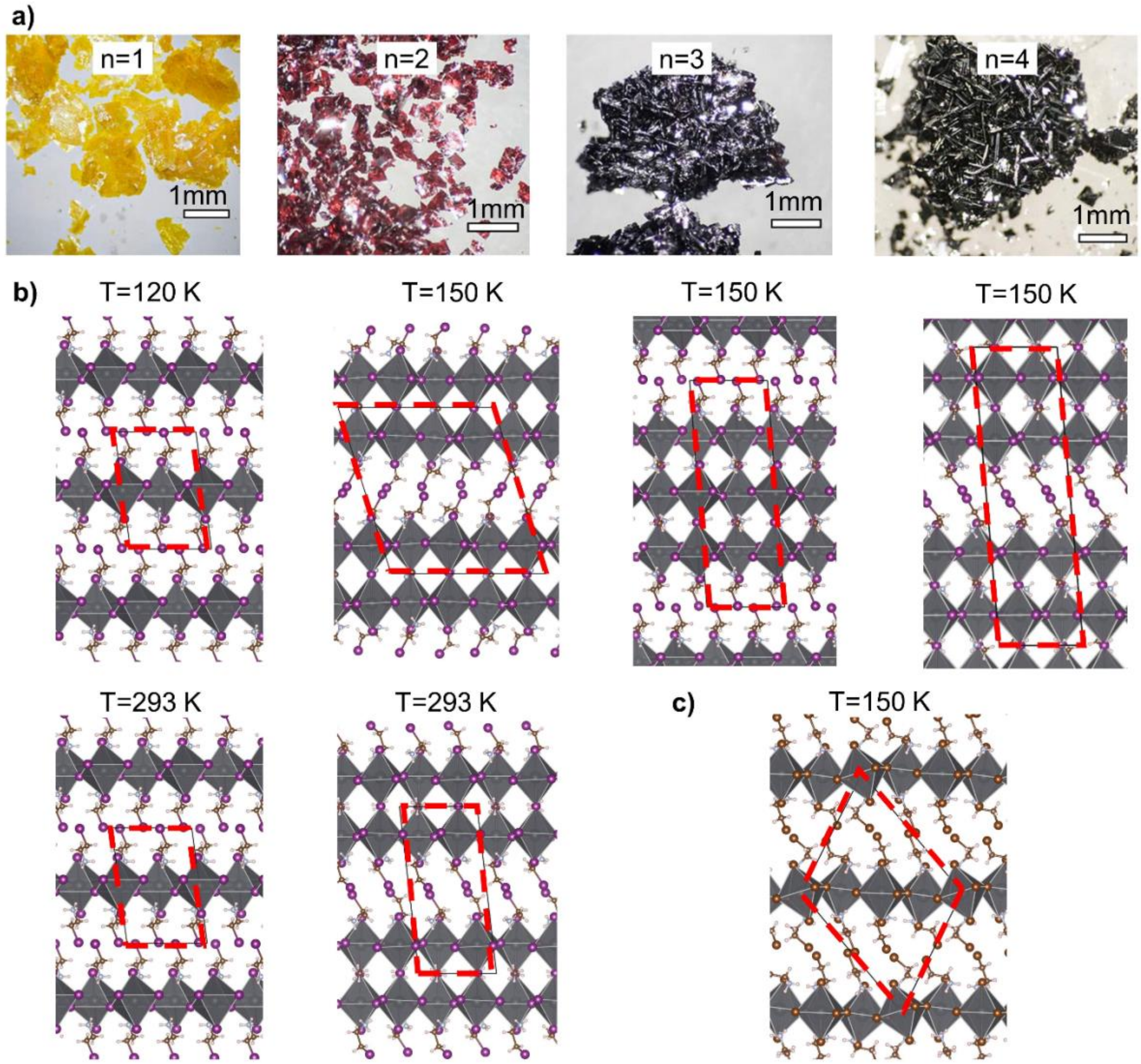

Figure 1. a) Pictures of the synthesized powders from optical microscopy; **b-c)** crystalline models for $(\mathrm{I\text{-}EA})_2\mathrm{MA}_{n-1}\mathrm{Pb}_n\mathrm{I3}_{n+1}$ (n=1,4) **(b)** and for $(\mathrm{Br\text{-}EA})_2\mathrm{PbBr}_4$ **(c)** layered halide perovskites obtained from XRD measurements. Crystalline cell (red dashed lines), and temperature at which the XRD measurement is performed are detailed. Room temperature crystalline structure of n=1 $(\mathrm{I\text{-}EA})_2\mathrm{PbI}_4$ compound is taken from Ref. [25].

Results

Crystal structures. Successful synthesis of pure phase $(\mathrm{I\text{-}EA})_2\mathrm{MA}_{n-1}\mathrm{Pb}_n\mathrm{I}_{3n+1}$ (n=1,4) compounds, along with n=1 $(\mathrm{Br\text{-}EA})_2\mathrm{PbBr}_4$ compound, is demonstrated via XRD measurements (see Figures S1-5) and optical microscopy images in Figure 1a. These latter attest the good quality of our samples, with crystals of n=1-4 compounds presenting plate-like morphology, as expected for such layered perovskites, and homogeneous color. Resolved crystal structures are illustrated in Figure 1b and 1c, for the $(\mathrm{I\text{-}EA})_2\mathrm{MA}_{n-1}\mathrm{Pb}_n\mathrm{I}_{3n+1}$ (n=1,4) series and the $(Br\text{-}EA)_2PbBr_4$ compound, respectively. XRD characterization is performed at low temperature, between 120 K and 150 K. Only exceptions are for the n=2 compounds, where room temperature phase is also resolved, and for the n=1 compound, where the room temperature phase was originally reported in Ref.[25]

XRD measurements (Table 1) outline even-odd effect in the crystal symmetry, with n=1,3 systems belonging to monoclinic space group $P2_1/c$ while n=2,4 belonging to triclinic space group P-1, respectively. Plane stacking motif in our materials and interplanar distances are discussed in Figure 2a-b.[9] Plane stacking in layered perovskites is classified considering the reciprocal shift between two consecutive inorganic sheets,[35,36] with two limiting cases represented by Dion-Jacobson (DJ) and Ruddlessden-Popper (RP) structures, Figure 2a. Namely, DJ corresponds to null in-plane shift, with consecutive inorganic sheets in eclipsed configuration, while RP corresponds to relative in-plane shift by half PbI_6 octahedron along both the two pseudo-cubic directions, with consecutive inorganic sheets in staggered configuration (see Figure 2a). Intermediate cases of Alternating Cation Interlayer (ACI) stacking motif were also recently reported, where adjacent planes are shifted along only one of the two pseudo-cubic axes.[21,37] A recent work by Li *et al.* outlined a light-induced contraction of the interplanar distance in layered 2D halide perovskites and a consequent improvement of the vertical transport properties and PV performances. This however was observed only for the DJ and ACI case, while RP samples did not show any light-induced transport properties evolution,[9] then indicating the plane stacking motif as an important figure of merit in 2D halide perovskites. For our series, plane stacking is shown in Figure 2b, considering the low temperature phases of n=1 and n=2, as representative of compounds with monoclinic (n=1,3) and triclinic (n=2,4) lattices. For n=1,3, plane stacking can be considered at the limit of the DJ motif, with rigid shift between two consecutive inorganic sheets related just to the monoclinic angle β (Table 1), while for n=2,4, plane stacking corresponds to ACI. All compounds hence fall in the case where the out-of-plane contraction and corresponding light-induced improvement of vertical transport properties was observed.[9]

The shortest distance between apical iodines from adjacent layers sets around 6.6 Å, see Figure 2b, irrespective of the specific DJ/ACI stacking. Such distance is shorter than the one measured for reference BA_2PbI_4 perovskite (8.6 Å)[38] but still larger than champion PV-efficiency $(4AMP)(MA)_2Pb_3I_{10}$ perovskite (4.12 Å),[9] or recently reported <110> terminated $(FA)_3(HEA)_2Pb_3I_{11}$ (HEA=hydroxyethylammonium) layered perovskite (4.55 Å).[39] XRD measurements however highlight very short distance (between 3.8 Å and 4.2 Å) between the iodine atom from the inorganic frame and the one from the I-EA spacer, see Figure 2c, which is a hallmark of the present multilayered perovskite series.

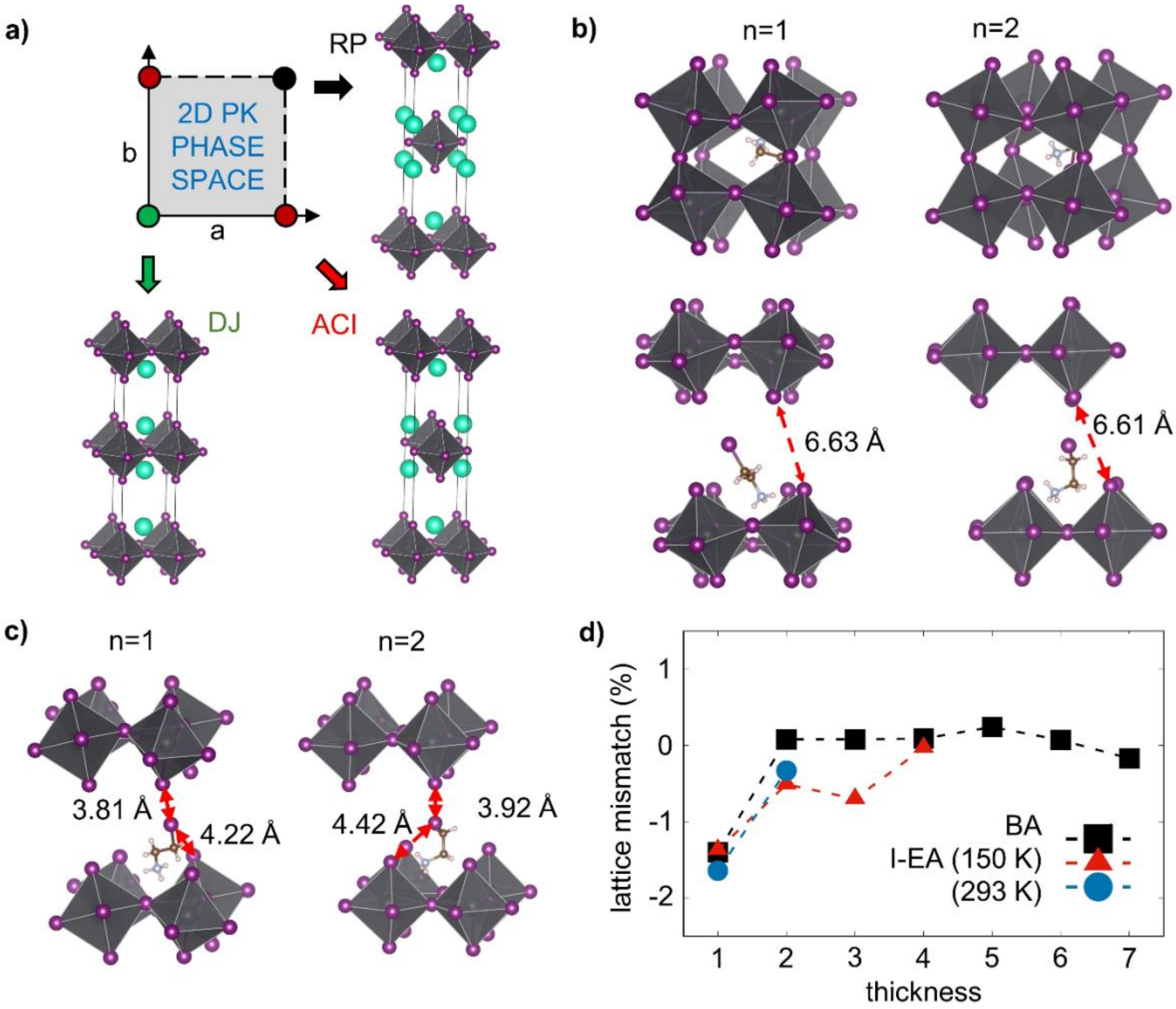

Figure 2. a) Classification of the plane stacking motifs in 2D halide perovskites (Dion-Jacobson- DJ, Alternating Cation Interlayer – ACI, Ruddlesden-Popper - RP); **b)** plane stacking and interlayer distance for low temperature polymorphs of n=1,2 compounds; **c)** interatomic distances between the iodine of the I-EA spacer and the closest iodines from the inorganic frame; **d)** in-plane lattice mismatch to $MAPbI_3$, as defined in Ref.[40], computed for the present multilayer perovskite series and for the butylammonium lead iodide series,[15] taken as reference.

Lattice mismatch for the inorganic and organic counterparts is also evaluated, following the approach proposed by Kepenekian *et al.*[40]. This compares the lattice parameters associated to the inorganic frame of layered compounds to that of the parental 3D perovskite material, to quantify the elastic strain associated to the interface with the organic spacer. Results are summarized in Figure 2d, and show that the lattice mismatch for the thinnest n=1 compound of the $(I\text{-}EA)_2MA_{n-1}Pb_nI_{3n+1}$ (around 1.4%) is comparable to that of the widely investigated butylammonium lead iodide compound, indicating overall modest strain.[40] Lattice mismatch further reduces for thicker compounds, hence explaining the favorable formation of multi-n layered perovskite structures in presence of I-EA organic spacer in terms of small organic-induced strain on the inorganic lattice.

For the sake of completeness, we extend the structural discussion also to previously reported $(Cl\text{-}EA)_2PbI_4$ and $(Br\text{-}EA)_2PbI_4$ analogues.[25] Here, we will briefly summarize the main distinguishing structural characteristics relevant to the present work. With X=Br and Cl, the plane stacking motif is of ACI type with shorter interlayer distances compared to Figure 2b (iodine-iodine distances as short as 5.07 Å and 4.84 Å, respectively, as shown in Figure S7). This is due to the specific orientation of the organic molecular backbone, which aligns parallel to the inorganic sheets whereas the halogens point almost perpendicularly, ensuring short intermolecular halide-halide distances of 3.80 Å for both Cl-EA and Br-EA spacers (see Figure S7). By contrast, I-EA cations align almost perpendicular to the plane stacking, leading the intermolecular iodine-iodine distances highlighted in Figure 2b. Meanwhile, the molecular iodine points towards the apical iodide of the perovskite layers (Figure 2c) leading to sizeable octahedral in-plane (~16° from linear bond) and out-of plane (~15° from the normal of the inorganic sheet) tilting as compared to the Br-EA and Cl-EA analogues for which tilt angles are small (deviation from linearity smaller than 4°). Considering the comparable average Pb-I bond lengths in all three structure, this octahedral tilting was associated to almost 200 meV blue shift in the UV-vis absorption of $I\text{-}EA_2PbI_4$ compared to the other two compounds.[25] Structural details for all compounds (bond length, bond valence angle, octahedral elongation and distortion indices, Baur parameter and σ_{oct}) are listed in Table S10.

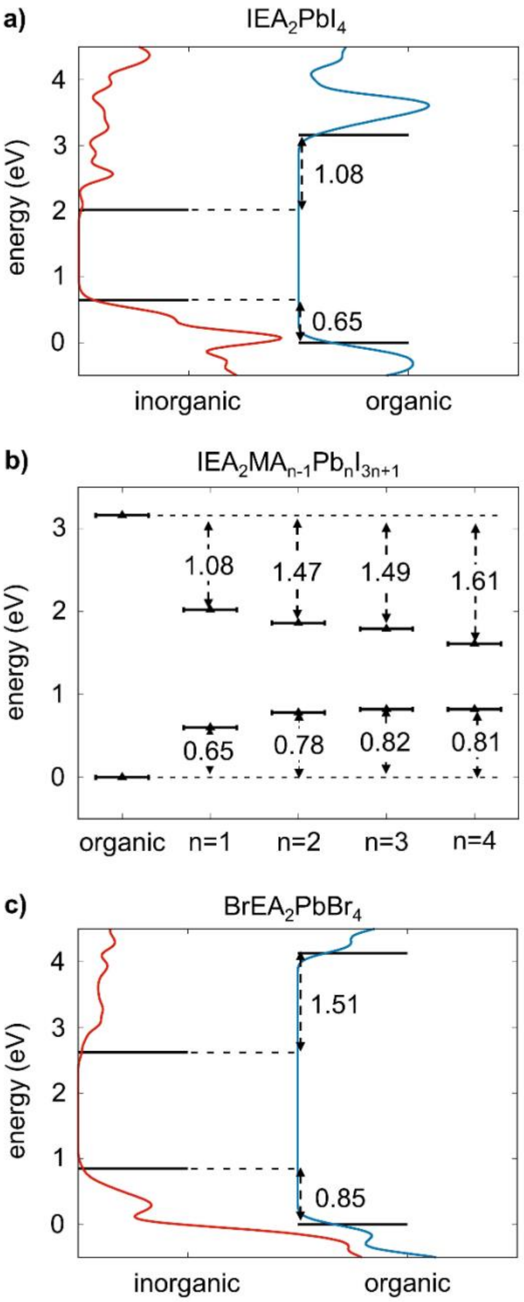

Figure 3. a) Electronic DOS for the inorganic and organic constituents of the n=1 (I-EA)$_2$PbI$_4$ layered halide perovskite, as obtained following the composite approach from Ref.[41]. The VBE/HOMO and CBE/LUMO offset are indicated; **b)** VBE/HOMO and CBE/LUMO offset for all compounds of the (I-EA)$_2$MA$_{n-1}$Pb$_n$I$_{3n+1}$ (n=1-4) series and for **c)** (Br-EA)$_2$PbBr$_4$ compounds.

Electronic structure. We performed DFT simulations to address the impact of the halide containing I-EA/Br-EA spacer on the electronic properties of these newly reported compounds. To first clarify the electronic level alignment at the organic/inorganic interface in the

$(I\text{-}EA)_2MA_{n-1}Pb_nI_{3n+1}$ series, we resorted to the composite approach proposed in Ref.[41]. This compares the electronic structure of the inorganic and organic constituents as computed separately, then reconstructing the alignment between the Valence/Conduction Band Edges (VBE/CBE) of the inorganic frame and the Highest Occupied/Lowest Unoccupied Molecular Orbital (HOMO/LUMO) of the spacer. Densities Of States (DOS) for the non-interacting inorganic/organic constituents in the thinnest n=1 $(I\text{-}EA)_2PbI_4$ compound in Figure 3a confirm the formation of type I quantum-well electronic interface, the band gap of the inorganic frame embedded in the one of the organic spacer. In presence of the halide containing I-EA spacer, however, holes/electrons are subject to a reduced confinement potential of 0.65/1.08 eV, compared to the reference case of n=1 butylammonium lead iodide compound (2.8/1.7 eV).[41] For thicker inorganic frames, the band gap closing originating from the less effective quantum confinement leads to larger VBE/HOMO and CBE/LUMO offset, as shown in Figure 3b. Finally, for the $(Br\text{-}EA)_2PbBr_4$ compound, substitution of iodine with bromine leads to comparable increase in the single particle gap for both the inorganic and organic constituents, (Figure 3c) hence leading to similar potential barrier (0.85/1.51 eV) found for $(I\text{-}EA)_2PbI_4$.

Single particle band structures for all compounds are shown in Figure 4. All newly synthesized layered perovskites present direct band gap at the center of the Brillouin zone (Γ), with corresponding band structures reflecting the quantum confinement for charge carriers. Namely, large dispersion is found along the reciprocal directions associated to the inorganic Pb_nI_{3n+1} sheet (Z→Γ / X→ Γ for n=1,3 / n=2,4 and $(Br\text{-}EA)_2PbBr_4$), while narrow dispersion is found along the plane-stacking direction (Γ→B or Γ→Z / Γ →T for n=1,3 / n=2,4 and for $(Br\text{-}EA)_2PbBr_4$,). Most notably, for all $(I\text{-}EA)_2MA_{n-1}Pb_nI_{3n+1}$ compounds, the valence and conduction bands along the plane stacking direction are not flat but show ca. tens of meV dispersion, hence indicating small electronic interaction between adjacent planes, in spite of quantum and dielectric confinement. In contrast, for $(Br\text{-}EA)_2PbBr_4$, both valence and conduction bands are flat.

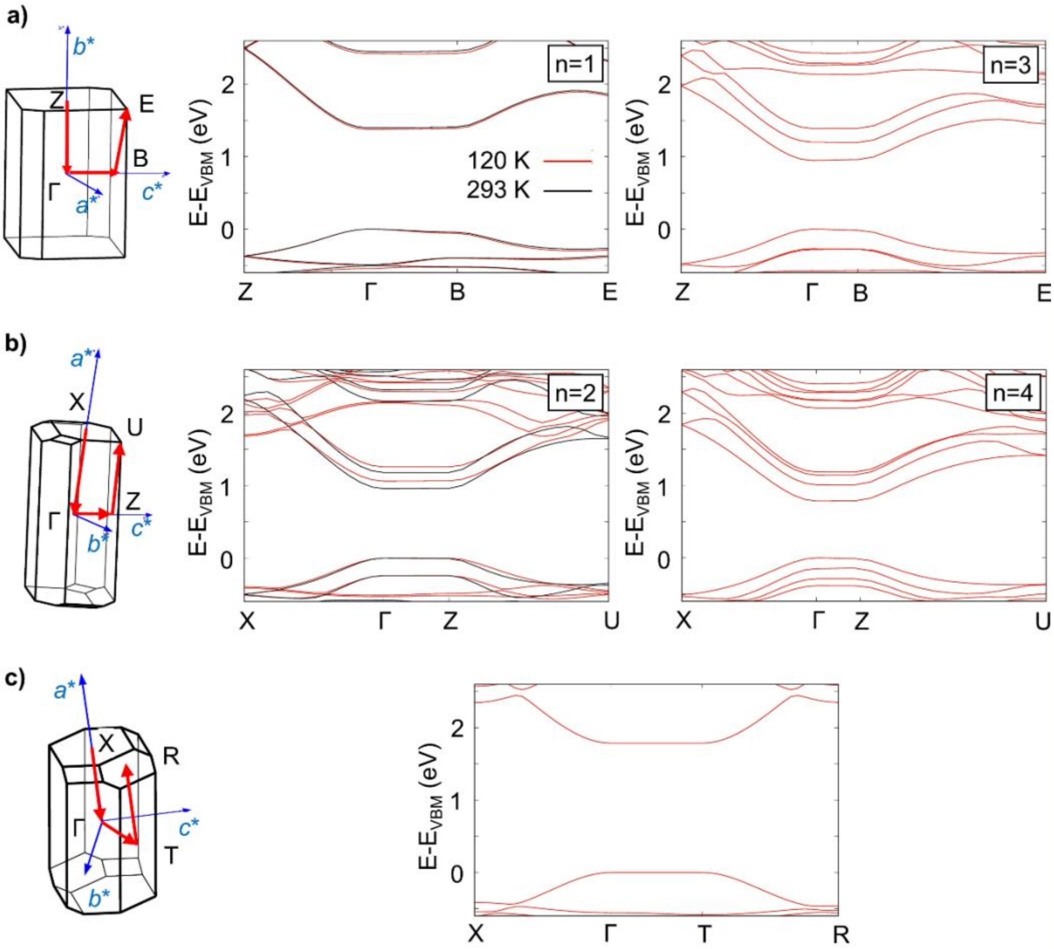

Figure 4. a-b) First Brillouin zone, high symmetry points path and corresponding band dispersion for the various compounds of the (I-EA)$_2$MA$_{n-1}$Pb$_n$I$_{3n+1}$ series; **a)** n=1 (both phases at T=120 K and T=293 K) and n=3 perovskites, all crystallizing with monoclinic lattice; **b)** n=2 (both phases at T=150 K and T=293 K) and n=4 perovskites, all crystallizing with triclinic lattice; **c)** Same for the (Br-EA)$_2$PbBr$_4$, compound, crystallizing with triclinic lattice. Brown color is for low temperature phases.

For the two polymorphs of the n=2 compound, DFT predicts 10 meV band gap difference, that can be tracked back to detailed structural features of the inorganic network. Previous investigations in fact highlighted the role of the octahedral rotations in modulating the electronic properties of halide perovskites, with distortions from the archetypal, undistorted P4mmm structure inducing less effective atomic hybridization,[42,43] then valence and conduction band narrowing, band gap opening and enhancement of the carrier effective masses.[44] For the case of the two (I-EA)$_2$MAPb$_2$I$_7$ (n=2) polymorphs, we found indeed a decrease of the average Pb-I-Pb distortion from 158 to 162 degrees, from the low to the room temperature phase, respectively, hence explaining the band gap closing computed for the latter (see Table S10).[43] On the same ground, the very close band gap found for the two polymorphs of the thinnest $(I\text{-}EA)_2PbI_4$ (n=1) compound reflects very similar structural features, the average bond length and valence bond angle differing for around 0.02 Å and 0.5 degrees (Table S10).

Superlattice effects related to halide containing short organic monocations. Motivated by the emergence of interlayer electronic interaction from the band dispersions in Figure 4, we proceeded to quantify it, by estimating the diagonal component of the hole/electron effective mass tensor associated to the plane stacking direction. For the low temperature phase of n=1, $(I\text{-}EA)_2PbI_4$ compound, holes/electrons effective masses amount to 1.8/8.3 m_e (m_e=electron masses), in striking contrast with the infinitely heavy carrier masses found for hexylammonium/dodecylammonium lead iodide compounds (∞).[42] Effective masses are modest in particular for holes, but reach values comparable to those computed for some performant organic semiconductors, as rubrene,[29] and BTBT derivatives.[30] Also electron effective mass slightly decreases compared to traditional alkylammonium-based lead iodide perovskites but remains larger compared to holes. The reason behind this unbalanced transport is easily addressed via group theory-based symmetry-analysis.[45,46] This in fact highlights that apical iodines contribute to formation of the VBE via the p_z orbitals (z corresponding to the plane stacking direction), while contribute to the formation of the CBE via the in-plane polarized p_{xy} orbitals, whose orientation does not allow an effective hybridization of Bloch states of adjacent inorganic sheets.[45]

Most important, the improved interlayer communication in the $(I\text{-}EA)_2MA_{n-1}Pb_nI_{3n+1}$ series (Figure 4) can be directly associated to the presence of the iodine from the spacer. To show this, we perform a computational experiment considering the low temperature phase of n=1, $(I\text{-}EA)_2PbI_4$ layered perovskite, as reference, then substituting the iodine from the I-EA spacer with Br, Cl and finally with CH_3, as in Figure 5a, and recomputing the band dispersion. At interplanar distance fixed to the experimental value, progressive $I \rightarrow Br \rightarrow Cl \rightarrow CH_3$ substitution leads in fact to flatter bands, as shown in Figure 5b, hence demonstrating the specific role of the halide from the spacer in the interlayer electronic interaction. Another evidence of this direct role from the spacer comes from the appearance of the band gap at the center of the Brillouin zone (Γ) instead than at the border (see Figure 4). Substitution of the iodine from the spacer with a CH_3 and subsequent reduction of the interlayer distance by half Angstrom leads in fact to band dispersion with band gap in B, as in Figure 5c. With focus on the valence, band edge destabilization in B can be simply understood in terms of the anti-bonding hybridization of the states of adjacent layers as in Figure 5c, peculiar of this point of the Brillouin zone. The incorporation of a iodine in the spacer leads to a different situation, as its atomic states contribute to the valence band hybridization and lead to the anti-bonding hybridization already in Γ, as in Figure 5d. In other words, the iodine from the I-EA spacer adds enough flexibility to form an anti-bonding hybridization pattern already at the center of the Brillouin zone.

Effective masses of n=2-4 compounds from the series can be also evaluated. For the thickest reference n=4 compound, out-of-plane hole/electron effective masses amount to 1.6/3.0 m_e. These modest values for the carrier effective masses however should not be straightforwardly associated to improved out-of-plane transport, as they also reflect the decreased quantum confinement in *n*=4 thick inorganic sheet.

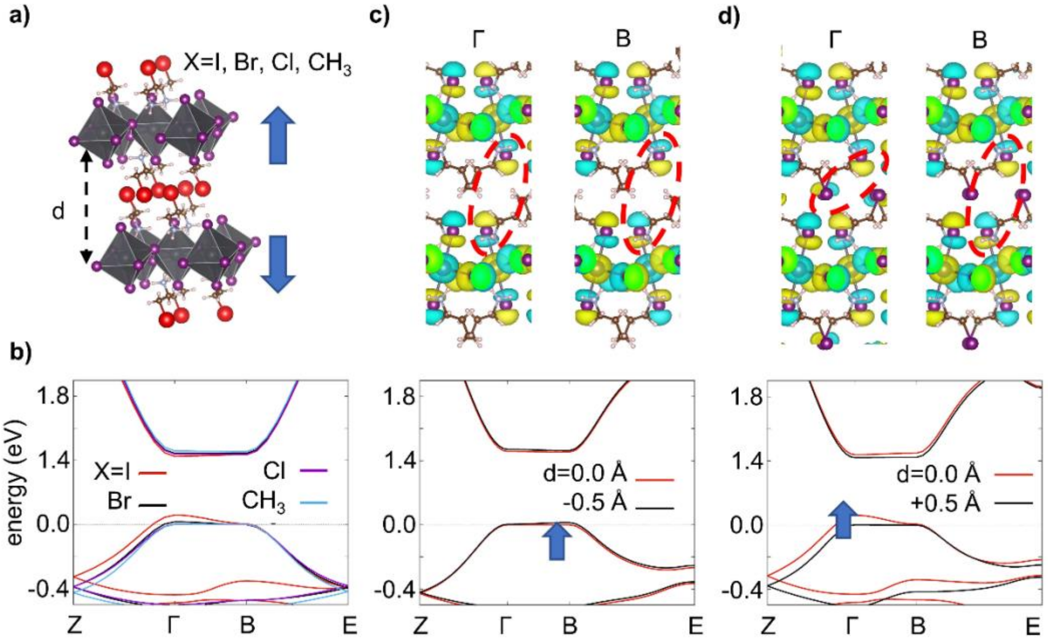

Figure 5. a) Schematics of the computational experiment highlighting the direct role of the I-EA spacer in enhancing the vertical transport. Given the low temperature structure of (I-EA)$_2$PbI$_4$, as reference, we tune both the composition of the spacer (X) and the interplanar distance (d); **b)** PBE+SOC band structure for (XEA)$_2$PbI$_4$ with X=CH$_3$, Br, Cl, I, at interplanar distance fixed to the experimental value; **c)** band structure for CH$_3$ substituted (X-EA)$_2$PbI$_4$, for interplanar distance as in the experiment (d=0.0 Å) and reduced by 0.5 Å (-0.5 Å). Isosurface associated to the VBE orbital at the Γ and B point of the Brillouin zone are also reported; **d)** same for (I-EA)$_2$PbI$_4$, with inteplanar distance as in the experiment and increased by 0.5 Å. Orbital isosurface set to 2.5 10^{-4} e/Bohr^3).

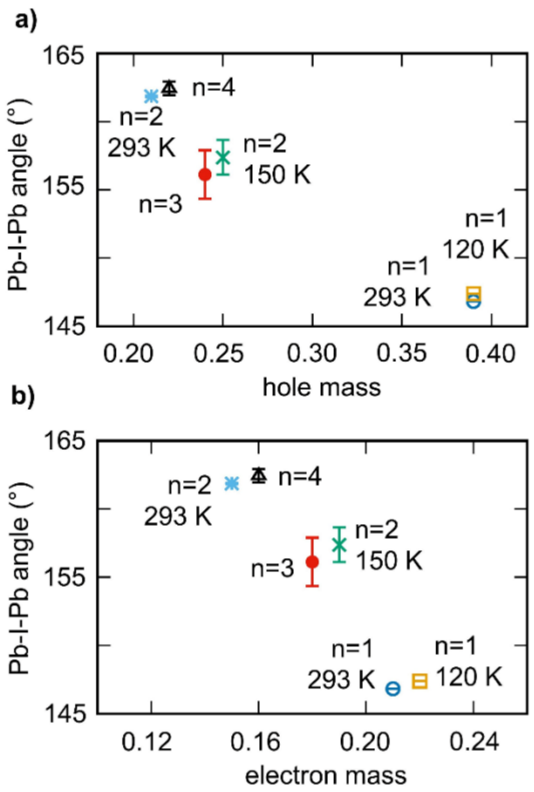

Figure 6. a) Hole and **b)** electron, in-plane effective masses computed for the $(\text{I-EA})_2\text{MA}_{n-1}\text{Pb}_n\text{I3}_{n+1}$ (n=1-4) compounds, as functions of the average Pb-I-Pb valence bond angles (vertical error-bars are associated to the standard deviation of the Pb-I-Pb angles). Effective masses are averaged along the two reciprocal directions associated to the in-plane lattice parameters.

In-plane transport properties. We complete the present analysis by estimating in-plane carrier effective masses, charge diffusion within the inorganic sheet representing the dominating mechanism for charge transport mobility in layered perovskite-based devices.[12,20] For the low temperature phase of thinnest $(\text{I-EA})_2\text{PbI}_4$ compound, these amount to 0.39/0.22 m_e, for holes/electrons. These values parallel previous estimates for dodecylammonium layered lead iodide perovskite in low temperature monoclinic phase (0.35/0.24 for holes/electrons)[42], while overcome those computed for 3D MAPbI_3 analogue along the corresponding crystallographic direction (0.22/0.16, as evaluated at the same PBE+SOC theory level).[47] The expectation is therefore that effective masses smoothly decrease with increasing thickness of the inorganic frame, bridging from the heavy masses of the thinnest n=1 compound to the lighter ones of the parental 3D material. This however is not the case for our compounds, with champion, room-temperature polymorph of n=2 showing smaller effective masses (0.21/0.15 for holes/electrons) than thicker n=3 (0.24/0.18) compound. The evolution of the in-plane effective mass is better understood when represented against the average Pb-I-Pb angle measured for the inorganic frame, as in Figure 6. In this case, we find in fact that more distorted structures are characterized by heavier charge carriers, as already discussed in the literature.[25,42–44] In this perspective, the dependence of the effective masses with respect to the inorganic thickness is thus indirect and mediated by structural distortions.

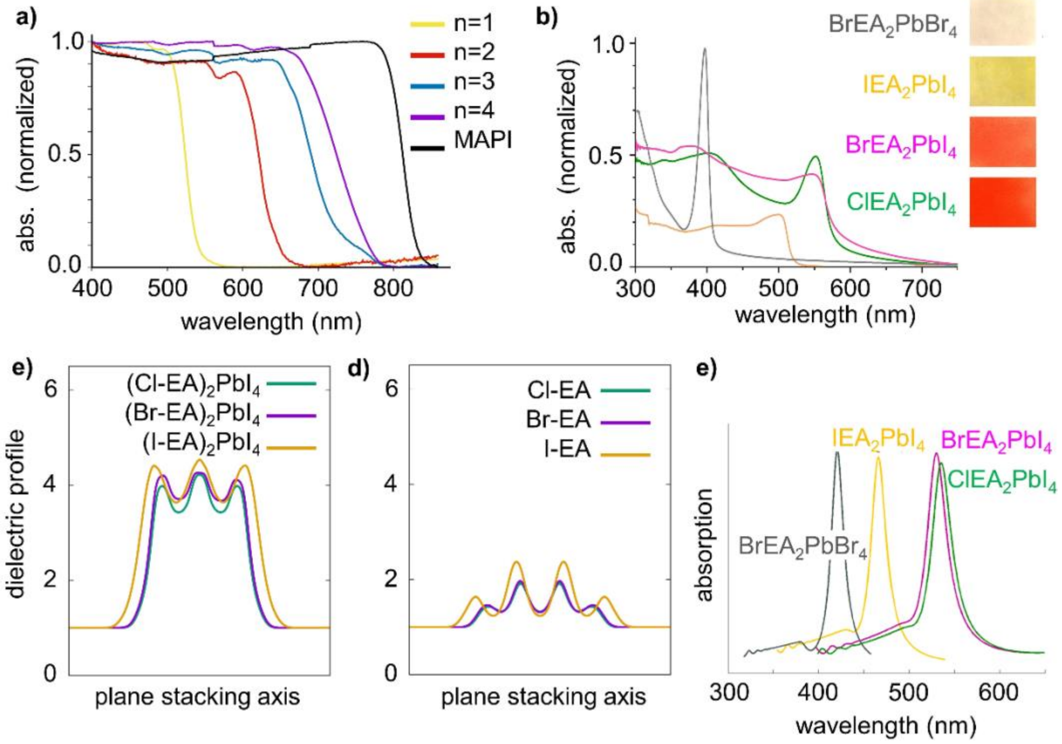

Figure 7. a) UV-vis absorption spectra of crystalline powders of $(\text{I-EA})_2\text{MA}_{n-1}\text{Pb}_n\text{I3}_{n+1}$ (n=1,4) compounds; **b)** UV-vis absorption spectra of thin films of $(\text{X-EA})_2\text{PbX'}_4$ (X=Cl, Br, I and X'=Br, I) compounds; **c)** dielectric profiles along the plane stacking direction for the $(\text{X-EA})_2\text{PbI}_4$ (X=Cl, Br, I) compounds and **d)** for the organic X-EA (X=Cl, Br, I) compounds; **e)** theoretical absorption spectra from semiempirical BSE calculations.

Optical properties. With potential focus on the exploitation of this novel series in photovoltaics, we performed UV-vis absorption characterization. The absorption spectra of crystalline powders in Figure 7a show the expected blue-shift of the excitonic absorption with decreasing thickness of the inorganic frame, reflecting the enhancement in quantum confinement effects. The absorption on-set for the n=3 compound shows a small shoulder, which may be indicative of a partial mixing between the n=3 and n=4 phases. Tauc plot analysis (Figure S8) provides estimates for the optical band gaps of 2.38 eV (n=1), 1.98 eV (n=2), 1.79 eV (n=3) and 1.71 eV (n=4). Our GGA+SOC electronic band structures in Figure 5 correctly reproduce the red-shift of the absorption on-set from thinnest n=1 compound (1.38 eV) to thickest one (0.79 eV). Accurate reproduction of the red-shift is however out-of-reach for DFT, as this does not account for electron-hole interaction, hence not catching the excitonic properties and the decrease of the exciton binding energy with increase of thickness “n”. In sight of potential exploitation of these materials in devices, we also proceeded with the synthesis and characterization of thin-films. Film homogeneity and lack of pinholes in the images obtained from optical microscopy from Figure S9 clearly attests a good control over materials morphology, while UV-vis absorption also shows the expected decrease of the optical gap with increasing the thickness of the inorganic layer. Notably, the optical gap found for thin-films of n=3,4 compounds are slightly red-shifted, compared to those of crystal powders, which may suggest the presence of thicker (n>4) phases, as already pointed out in the literature. Preparation of thin-films of the $(I\text{-}EA)_2MA_{n-1}Pb_nI_{3n+1}$ (n=1-4) compounds is hence demonstrated, although additional synthetic and characterization efforts are required, to optimize the film morphology and control over phase purity.

To clarify the influence on the optical properties due to the halide from both the inorganic backbone and, more important, from the spacer, we analyzed UV-vis spectra of n=1 $(X\text{-}EA)_2PbX'_4$ compounds at RT, where X=I/Br/Cl and X’=I/Br (Figure 7b). As expected, the substitution of the bromine by iodine in the perovskite backbone of $(Br\text{-}EA)_2PbBr_4$ leads to a red shift of the optical band gap.[10] Dealing with the halide from the spacer, 250 meV blue-shift in the optical spectrum is found in Figure 7b when going from $(Cl\text{-}EA)_2PbI_4$ and $(Br\text{-}EA)_2PbI_4$ to $(I\text{-}EA)_2PbI_4$. In original Ref.[25], this was mainly associated to structural effects, namely spacer-induced distortion in the inorganic frame of the latter compound. Consistently, our DFT calculations confirm 390 meV band gap opening from less distorted $(Cl\text{-}EA)_2PbI_4$ and $(Br\text{-}EA)_2PbI_4$ to more distorted $(I\text{-}EA)_2PbI_4$. (see Table S10). On the other hand, additional effects from the I-EA spacer cannot be ruled out, considering the polarizability of iodine, in line with the findings by Smith et al.[27] We therefore performed additional DFT calculations on the $(X\text{-}EA)_2PbI_4$ compounds (X=Cl, Br, I), aiming to clarify the dielectric properties of these hybrid as function of the halide in the interlayer space. Results in Figure 7c do not highlight dielectric inversion as in Ref. [27], but clearly show decreased dielectric contrast between the inorganic and the organic constituents, due to the increase in the dielectric constant from the latter, as evidenced in Figure 7d, from 2.0 to 2.4, for $(Br\text{-}EA)_2PbI_4$ and $(I\text{-}EA)_2PbI_4$, respectively. As known both experimentally and theoretically,[34] the reduction of the dielectric constant mismatch leads in turn to a reduction of the exciton binding energy and oscillator strength. The dielectric profile for pure brominated compound is also estimated (see Figure S10), showing a decrease in the dielectric constant, compared to iodine based compounds.[48,41]

The large crystalline cell of 2D perovskites hinders the possibility to perform first principle calculations targeting the excitonic properties of these materials, and only few simulations based on the ab-initio solution of the Bethe-Salpeter equation (BSE) have been reported, thus far.[49–54] A semi-empirical implementation of the BSE for a Wannier-Mott exciton is nevertheless possible.[34] The simulations of the optical absorption spectra (Figure 7e) are only valid close to the respective band gaps and exciton resonances. To visually offer a better match with experimental spectra, an energy shift of 1.5eV is added on top of all the DFT computed electronic band gaps. Still, the same homogeneous broadening is considered for all compositions, while experimental spectra strongly depend on the quality of the thin films and exhibit very different inhomogeneous broadenings (Figure 7b). Results show that for the (X-EA)$_2$PbI$_4$ compounds, the positions of the optical band gaps are essentially dominated by the influence of the distortions of the perovskite lattice on the electronic band gaps.[25]

Conclusions

With mixed 2D/3D halide perovskite-based architectures emerging as a promising solution for performant and stable halide perovskite-based photovoltaics, there has been growing effort in synthesizing novel 2D layered compounds,[11,12] especially the thicker (n=3,4) ones, that may guarantee a good interaction with the underlying 3D component.[17,18] Here, we report the synthesis of new 2D (I-EA)$_2$MA$_{n-1}$Pb$_n$I$_{3n+1}$ (n=1,4) and (Br-EA)$_2$PbBr$_4$ perovskite compounds, the phase purity being demonstrated via powder XRD diffraction measurements. All compounds feature halide containing iodo-ethylammonium (I-EA) or bromo-ethylammonium (Br-EA), which very likely contribute to the successful formation of layered perovskite structure for the full n=1,4 series, thanks to the modest lattice strain associated to the organic/inorganic interface, comparable to the one of reference butylammonium (BA)$_2$MA$_{n-1}$Pb$_n$I$_{3n+1}$ lead iodide perovskite series.[40] The incorporation of heavy halides (Br or I) in the interlayer region of 2D halide perovskites has been widely exploited in the literature,[25–27] but is known to impact on the material properties, in particular the dielectric confinement,[27] and the optical properties of these hybrids.[25] Here, our DFT calculations confirm these effects, indicating reduced dielectric contrast between the inorganic frame and the organic spacer, which should reflect in increased exciton screening and ease electron-hole separation. Most notably, DFT calculations suggest the direct involvement of the I-EA spacer in the interplanar electronic coupling for these hybrids, leading to effective masses for hole carriers along the plane stacking direction of 1.8 m_e, considerably reduced compared to those of alkylammonium lead iodide compounds,[42] and closely matching those of popular organic semiconductors.[29] Optical UV-vis characterization sets the absorption onset for the n=3,4 perovskites thin films around 1.71 eV, hence nicely paralleling champion photovoltaic efficiency $(4AMP)MA_2Pb_3I_{10}$ 2D halide perovskite.[9] Therefore, thanks to the good-phase control also for the thicker n=3,4 components, we propose these new $(I\text{-}AE)_2MA_{n-1}Pb_nI_{3n+1}$ layered compounds as potential candidates for 2D/3D halide perovskite-based photovoltaic devices. In addition, we suggest the incorporation of halides species in the interlayer, in particular of iodine, as design rule for multilayered halide perovskite materials with improved vertical transport and more-effective electron-hole separation. Inspired by this design concept, also multi-n compounds with different halides in the organic and inorganic components and full-Br and full-Cl multi-n compounds can be considered for future studies, with potential development of materials with engineered dielectric-contrast and excitonic properties. These will likely require careful tuning of the synthetic approaches, as for instance the current exploitation of HI solutions may lead to rapid halide substitution, in the case of compounds with different halide in the spacer and in the perovskite lattice.

ACKNOWLEDGEMENT

The work at ISCR and MOLTECH-Anjou was mainly supported by the Agence Nationale pour la Recherche (MORELESS project). For DFT calculations, this work was granted access to the HPC resources of TGCC/CINES/IDRIS under the allocation 2020-A0090907682 made by GENCI. C.Q. is FNRS research associate. J.E. acknowledges the financial support from the Institut Universitaire de France. Part of the work at ISCR and Institut FOTON was funded by the European Union's Horizon 2020 research and innovation program under grant agreement no. 861985 (PeroCUBE). CQ warmly thanks Dr. Mikael Kepenekian and Dr. Boubacar Traore for technical support in the calculations of the dielectric profiles.

Supporting Information. Details for the synthesis of $(I\text{-}C_2H_4\text{-}NH_3)_2(CH_3NH_3)_{n-1}[Pb_nI_{3n+1}]$ crystal powders; details for the synthesis of $(I\text{-}C_2H_4\text{-}NH_3)_2(CH_3NH_3)_{n-1}[Pb_nI_{3n+1}]$ thin films; powder XRD characterization; ^1H NMR characterization in solution; resolved crystal structures; computational details; structural analysis; Tauc plot analysis for powders; optical absorption and morphology of thin-films; comparison of the dielectric profile for bromine and iodine-based compounds. Crystal Information Files of the synthesized compounds are deposited on the CCDC, with numbers 2223697 (n= 1); 2223698 and 2223699 (n= 2 RT and 150 K); 2223700 (n= 3); 2223702 (n= 4) and 2223701 ($(BrEA)_2PbBr_4$).

References

(1) Yang, R.; Li, R.; Cao, Y.; Wei, Y.; Miao, Y.; Tan, W. L.; Jiao, X.; Chen, H.; Zhang, L.; Chen, Q.; Zhang, H.; Zou, W.; Wang, Y.; Yang, M.; Yi, C.; Wang, N.; Gao, F.; McNeill, C. R.; Qin, T.; Wang, J.; Huang, W. Oriented Quasi-2D Perovskites for High Performance Optoelectronic Devices. *Advanced Materials* **2018**, *30* (51), 1804771. https://doi.org/10.1002/adma.201804771.

(2) Yuan, S.; Wang, Z.-K.; Xiao, L.-X.; Zhang, C.-F.; Yang, S.-Y.; Chen, B.-B.; Ge, H.-T.; Tian, Q.-S.; Jin, Y.; Liao, L.-S. Optimization of Low-Dimensional Components of Quasi-2D Perovskite Films for Deep-Blue Light-Emitting Diodes. *Advanced Materials* **2019**, *31* (44), 1904319. https://doi.org/10.1002/adma.201904319.

(3) Sun, C.; Jiang, Y.; Cui, M.; Qiao, L.; Wei, J.; Huang, Y.; Zhang, L.; He, T.; Li, S.; Hsu, H.-Y.; Qin, C.; Long, R.; Yuan, M. High-Performance Large-Area Quasi-2D Perovskite Light-Emitting Diodes. *Nat Commun* **2021**, *12* (1), 2207. https://doi.org/10.1038/s41467-021-22529-x.

(4) Yuan, M.; Quan, L. N.; Comin, R.; Walters, G.; Sabatini, R.; Voznyy, O.; Hoogland, S.; Zhao, Y.; Beauregard, E. M.; Kanjanaboos, P.; Lu, Z.; Kim, D. H.; Sargent, E. H. Perovskite Energy Funnels for Efficient Light-Emitting Diodes. *Nature Nanotech* **2016**, *11* (10), 872–877. https://doi.org/10.1038/nnano.2016.110.

(5) Birowosuto, M. D.; Cortecchia, D.; Drozdowski, W.; Brylew, K.; Lachmanski, W.; Bruno, A.; Soci, C. X-Ray Scintillation in Lead Halide Perovskite Crystals. *Sci Rep* **2016**, *6* (1), 37254. https://doi.org/10.1038/srep37254.

(6) Duong, T.; John, A. T.; Chen, H.; Pham, H.; Murugappan, K.; Tran-Phu, T.; Tricoli, A.; Catchpole, K. Mixed-Dimensional Organic–Inorganic Metal Halide Perovskite (OIMHP) Based Gas Sensors with Superior Stability for NO_2 Detection. *Mater. Adv.* **2022**, *3* (2), 1263–1271. https://doi.org/10.1039/D1MA00976A.

(7) Grancini, G.; Roldán-Carmona, C.; Zimmermann, I.; Mosconi, E.; Lee, X.; Martineau, D.; Narbey, S.; Oswald, F.; De Angelis, F.; Graetzel, M.; Nazeeruddin, M. K. One-Year Stable Perovskite Solar Cells by 2D/3D Interface Engineering. *Nat Commun* **2017**, *8* (1), 15684. https://doi.org/10.1038/ncomms15684.

(8) Grancini, G.; Nazeeruddin, M. K. Dimensional Tailoring of Hybrid Perovskites for Photovoltaics. *Nat Rev Mater* **2019**, *4* (1), 4–22. https://doi.org/10.1038/s41578-018-0065-0.

(9) Li, W.; Sidhik, S.; Traore, B.; Asadpour, R.; Hou, J.; Zhang, H.; Fehr, A.; Essman, J.; Wang, Y.; Hoffman, J. M.; Spanopoulos, I.; Crochet, J. J.; Tsai, E.; Strzalka, J.; Katan, C.; Alam, M. A.; Kanatzidis, M. G.; Even, J.; Blancon, J.-C.; Mohite, A. D. Light-Activated Interlayer Contraction in Two-Dimensional Perovskites for High-Efficiency Solar Cells. *Nat. Nanotechnol.* **2022**, *17* (1), 45–52. https://doi.org/10.1038/s41565-021-01010-2.

(10) Katan, C.; Mercier, N.; Even, J. Quantum and Dielectric Confinement Effects in Lower-Dimensional Hybrid Perovskite Semiconductors. *Chem. Rev.* **2019**, *119* (5), 3140–3192. https://doi.org/10.1021/acs.chemrev.8b00417.

(11) Sidhik, S.; Wang, Y.; De Siena, M.; Asadpour, R.; Torma, A. J.; Terlier, T.; Ho, K.; Li, W.; Puthirath, A. B.; Shuai, X.; Agrawal, A.; Traore, B.; Jones, M.; Giridharagopal, R.; Ajayan, P. M.; Strzalka, J.; Ginger, D. S.; Katan, C.; Alam, M. A.; Even, J.; Kanatzidis, M. G.; Mohite, A. D. Deterministic Fabrication of 3D/2D Perovskite Bilayer Stacks for Durable and Efficient Solar Cells. *Science* **2022**, *377* (6613), 1425–1430. https://doi.org/10.1126/science.abq7652.

(12) Tsai, H.; Nie, W.; Blancon, J.-C.; Stoumpos, C. C.; Asadpour, R.; Harutyunyan, B.; Neukirch, A. J.; Verduzco, R.; Crochet, J. J.; Tretiak, S.; Pedesseau, L.; Even, J.; Alam, M. A.; Gupta, G.; Lou, J.; Ajayan, P. M.; Bedzyk, M. J.; Kanatzidis, M. G.; Mohite, A. D. High-Efficiency Two-Dimensional Ruddlesden–Popper Perovskite Solar Cells. *Nature* **2016**, *536* (7616), 312–316. https://doi.org/10.1038/nature18306.

(13) Calabrese, J.; Jones, N. L.; Harlow, R. L.; Herron, N.; Thorn, D. L.; Wang, Y. Preparation and Characterization of Layered Lead Halide Compounds. *J. Am. Chem. Soc.* **1991**, *113* (6), 2328–2330. https://doi.org/10.1021/ja00006a076.

(14) Smith, I. C.; Hoke, E. T.; Solis-Ibarra, D.; McGehee, M. D.; Karunadasa, H. I. A Layered Hybrid Perovskite Solar-Cell Absorber with Enhanced Moisture Stability. *Angewandte Chemie International Edition* **2014**, *53* (42), 11232–11235. https://doi.org/10.1002/anie.201406466.

(15) Stoumpos, C. C.; Cao, D. H.; Clark, D. J.; Young, J.; Rondinelli, J. M.; Jang, J. I.; Hupp, J. T.; Kanatzidis, M. G. Ruddlesden–Popper Hybrid Lead Iodide Perovskite 2D Homologous Semiconductors. *Chem. Mater.* **2016**, *28* (8), 2852–2867. https://doi.org/10.1021/acs.chemmater.6b00847.

(16) Stoumpos, C. C.; Soe, C. M. M.; Tsai, H.; Nie, W.; Blancon, J.-C.; Cao, D. H.; Liu, F.; Traoré, B.; Katan, C.; Even, J.; Mohite, A. D.; Kanatzidis, M. G. High Members of the 2D Ruddlesden-Popper Halide Perovskites: Synthesis, Optical Properties, and Solar Cells of $(CH_3(CH_2)_3NH_3)_2(CH_3NH_3)_4Pb_5I_{16}$. *Chem* **2017**, *2* (3), 427–440. https://doi.org/10.1016/j.chempr.2017.02.004.

(17) Li, X.; Ke, W.; Traoré, B.; Guo, P.; Hadar, I.; Kepenekian, M.; Even, J.; Katan, C.; Stoumpos, C. C.; Schaller, R. D.; Kanatzidis, M. G. Two-Dimensional Dion–Jacobson Hybrid Lead Iodide Perovskites with Aromatic Diammonium Cations. *J. Am. Chem. Soc.* **2019**, *141* (32), 12880–12890. https://doi.org/10.1021/jacs.9b06398.

(18) Mao, L.; Ke, W.; Pedesseau, L.; Wu, Y.; Katan, C.; Even, J.; Wasielewski, M. R.; Stoumpos, C. C.; Kanatzidis, M. G. Hybrid Dion–Jacobson 2D Lead Iodide Perovskites. *J. Am. Chem. Soc.* **2018**, *140* (10), 3775–3783. https://doi.org/10.1021/jacs.8b00542.

(19) *Best Research-Cell Efficiency Chart.* https://www.nrel.gov/pv/cell-efficiency.html (accessed 2022-07-08).

(20) Cao, D. H.; Stoumpos, C. C.; Farha, O. K.; Hupp, J. T.; Kanatzidis, M. G. 2D Homologous Perovskites as Light-Absorbing Materials for Solar Cell Applications. *J. Am. Chem. Soc.* **2015**, *137* (24), 7843–7850. https://doi.org/10.1021/jacs.5b03796.

(21) Nazarenko, O.; Kotyrba, M. R.; Wörle, M.; Cuervo-Reyes, E.; Yakunin, S.; Kovalenko, M. V. Luminescent and Photoconductive Layered Lead Halide Perovskite Compounds Comprising Mixtures of Cesium and Guanidinium Cations. *Inorg. Chem.* **2017**, *56* (19), 11552–11564. https://doi.org/10.1021/acs.inorgchem.7b01204.

(22) Mitzi, D. B.; Chondroudis, K.; Kagan, C. R. Design, Structure, and Optical Properties of Organic−Inorganic Perovskites Containing an Oligothiophene Chromophore. *Inorg. Chem.* **1999**, *38* (26), 6246–6256. https://doi.org/10.1021/ic991048k.

(23) Gao, Y.; Shi, E.; Deng, S.; Shiring, S. B.; Snaider, J. M.; Liang, C.; Yuan, B.; Song, R.; Janke, S. M.; Liebman-Peláez, A.; Yoo, P.; Zeller, M.; Boudouris, B. W.; Liao, P.; Zhu, C.; Blum, V.; Yu, Y.; Savoie, B. M.; Huang, L.; Dou, L. Molecular Engineering of Organic–Inorganic Hybrid Perovskites Quantum Wells. *Nat. Chem.* **2019**, *11* (12), 1151–1157. https://doi.org/10.1038/s41557-019-0354-2.

(24) Lédée, F.; Audebert, P.; Trippé-Allard, G.; Galmiche, L.; Garrot, D.; Marrot, J.; Lauret, J.-S.; Deleporte, E.; Katan, C.; Even, J.; Quarti, C. Tetrazine Molecules as an Efficient Electronic Diversion Channel in 2D Organic–Inorganic Perovskites. *Mater. Horiz.* **2021**, *8* (5), 1547–1560. https://doi.org/10.1039/D0MH01904F.

(25) Sourisseau, S.; Louvain, N.; Bi, W.; Mercier, N.; Rondeau, D.; Boucher, F.; Buzaré, J.-Y.; Legein, C. Reduced Band Gap Hybrid Perovskites Resulting from Combined Hydrogen and Halogen Bonding at the Organic−Inorganic Interface. *Chem. Mater.* **2007**, *19* (3), 600–607. https://doi.org/10.1021/cm062380e.

(26) Chakraborty, R.; Sheikh, T.; Nag, A. Iodine–Iodine Interactions Suppressing Phase Transitions of 2D Layered Hybrid $(I\text{-}(CH_2)_n\text{-}NH_3)_2PbI_4$ (n = 2–6) Perovskites. *Chem. Mater.* **2022**, *34* (1), 288–296. https://doi.org/10.1021/acs.chemmater.1c03492.

(27) Smith, M. D.; Pedesseau, L.; Kepenekian, M.; Smith, I. C.; Katan, C.; Even, J.; Karunadasa, H. I. Decreasing the Electronic Confinement in Layered Perovskites through Intercalation. *Chem. Sci.* **2017**, *8* (3), 1960–1968. https://doi.org/10.1039/C6SC02848A.

(28) Sánchez-Carrera, R. S.; Atahan, S.; Schrier, J.; Aspuru-Guzik, A. Theoretical Characterization of the Air-Stable, High-Mobility Dinaphtho[2,3-b:2′3′-f]Thieno[3,2-b]-Thiophene Organic Semiconductor. *J. Phys. Chem. C* **2010**, *114* (5), 2334–2340. https://doi.org/10.1021/jp910102f.

(29) Gali, S. M.; Quarti, C.; Olivier, Y.; Cornil, J.; Truflandier, L.; Castet, F.; Muccioli, L.; Beljonne, D. Impact of Structural Anisotropy on Electro-Mechanical Response in Crystalline Organic Semiconductors. *J. Mater. Chem. C* **2019**, *7* (15), 4382–4391. https://doi.org/10.1039/C8TC06385K.

(30) Fijahi, L.; Salzillo, T.; Tamayo, A.; Bardini, M.; Ruzié, C.; Quarti, C.; Beljonne, D.; d'Agostino, S.; H. Geerts, Y.; Mas-Torrent, M. Charge Transfer Complexes of a Benzothienobenzothiophene Derivative and Their Implementation as Active Layer in Solution-Processed Thin Film Organic Field-Effect Transistors. *Journal of Materials Chemistry C* **2022**, *10* (18), 7319–7328. https://doi.org/10.1039/D2TC00655C.

(31) Giannozzi, P.; Baroni, S.; Bonini, N.; Calandra, M.; Car, R.; Cavazzoni, C.; Ceresoli, D.; Chiarotti, G. L.; Cococcioni, M.; Dabo, I.; Corso, A. D.; Gironcoli, S. de; Fabris, S.; Fratesi, G.; Gebauer, R.; Gerstmann, U.; Gougoussis, C.; Kokalj, A.; Lazzeri, M.; Martin-Samos, L.; Marzari, N.; Mauri, F.; Mazzarello, R.; Paolini, S.; Pasquarello, A.; Paulatto, L.; Sbraccia, C.; Scandolo, S.; Sclauzero, G.; Seitsonen, A. P.; Smogunov, A.; Umari, P.; Wentzcovitch, R. M. QUANTUM ESPRESSO: A Modular and Open-Source Software Project for Quantum Simulations of Materials. *J. Phys.: Condens. Matter* **2009**, *21* (39), 395502. https://doi.org/10.1088/0953-8984/21/39/395502.

(32) Soler, J. M.; Artacho, E.; Gale, J. D.; García, A.; Junquera, J.; Ordejón, P.; Sánchez-Portal, D. The SIESTA Method Forab Initioorder-Nmaterials Simulation. *J. Phys.: Condens. Matter* **2002**, *14* (11), 2745–2779. https://doi.org/10.1088/0953-8984/14/11/302.

(33) Even, J.; Pedesseau, L.; Kepenekian, M. Electronic Surface States and Dielectric Self-Energy Profiles in Colloidal Nanoscale Platelets of CdSe. *Phys. Chem. Chem. Phys.* **2014**, *16* (45), 25182–25190. https://doi.org/10.1039/C4CP03267E.

(34) Blancon, J.-C.; Stier, A. V.; Tsai, H.; Nie, W.; Stoumpos, C. C.; Traoré, B.; Pedesseau, L.; Kepenekian, M.; Katsutani, F.; Noe, G. T.; Kono, J.; Tretiak, S.; Crooker, S. A.; Katan, C.; Kanatzidis, M. G.; Crochet, J. J.; Even, J.; Mohite, A. D. Scaling Law for Excitons in

2D Perovskite Quantum Wells. *Nat Commun* **2018**, *9* (1), 2254. https://doi.org/10.1038/s41467-018-04659-x.

(35) Blancon, J.-C.; Even, J.; Stoumpos, C. C.; Kanatzidis, M. G.; Mohite, A. D. Semiconductor Physics of Organic–Inorganic 2D Halide Perovskites. *Nat. Nanotechnol.* **2020**, *15* (12), 969–985. https://doi.org/10.1038/s41565-020-00811-1.

(36) Marchenko, E. I.; Korolev, V. V.; Mitrofanov, A.; Fateev, S. A.; Goodilin, E. A.; Tarasov, A. B. Layer Shift Factor in Layered Hybrid Perovskites: Univocal Quantitative Descriptor of Composition–Structure–Property Relationships. *Chem. Mater.* **2021**, *33* (4), 1213–1217. https://doi.org/10.1021/acs.chemmater.0c03935.

(37) Soe, C. M. M.; Stoumpos, C. C.; Kepenekian, M.; Traoré, B.; Tsai, H.; Nie, W.; Wang, B.; Katan, C.; Seshadri, R.; Mohite, A. D.; Even, J.; Marks, T. J.; Kanatzidis, M. G. New Type of 2D Perovskites with Alternating Cations in the Interlayer Space, $(C(NH_2)_3)(CH_3NH_3)_nPb_nI_{3n+1}$: Structure, Properties, and Photovoltaic Performance. *J. Am. Chem. Soc.* **2017**, *139* (45), 16297–16309. https://doi.org/10.1021/jacs.7b09096.

(38) Billing, D. G.; Lemmerer, A. Synthesis, Characterization and Phase Transitions in the Inorganic–Organic Layered Perovskite-Type Hybrids $[(C_nH_{2n+1}NH_3)_2PbI_4]$, n = 4, 5 and 6. *Acta Cryst B* **2007**, *63* (5), 735–747. https://doi.org/10.1107/S0108768107031758.

(39) Ben Haj Salah, M.; Mercier, N.; Allain, M.; Leblanc, A.; Dittmer, J.; Botta, C.; Quarti, C.; Katan, C. Synthesis and Characterization of $(FA)_3(HEA)_2Pb_3I_{11}$: A Rare Example of <1 1 0>-Oriented Multilayered Halide Perovskites. *Chem. Mater.* **2022**, *34* (13), 5780–5790. https://doi.org/10.1021/acs.chemmater.2c00130.

(40) Kepenekian, M.; Traore, B.; Blancon, J.-C.; Pedesseau, L.; Tsai, H.; Nie, W.; Stoumpos, C. C.; Kanatzidis, M. G.; Even, J.; Mohite, A. D.; Tretiak, S.; Katan, C. Concept of Lattice Mismatch and Emergence of Surface States in Two-Dimensional Hybrid Perovskite Quantum Wells. *Nano Lett.* **2018**, *18* (9), 5603–5609. https://doi.org/10.1021/acs.nanolett.8b02078.

(41) Traore, B.; Pedesseau, L.; Assam, L.; Che, X.; Blancon, J.-C.; Tsai, H.; Nie, W.; Stoumpos, C. C.; Kanatzidis, M. G.; Tretiak, S.; Mohite, A. D.; Even, J.; Kepenekian, M.; Katan, C. Composite Nature of Layered Hybrid Perovskites: Assessment on Quantum and Dielectric Confinements and Band Alignment. *ACS Nano* **2018**, *12* (4), 3321–3332. https://doi.org/10.1021/acsnano.7b08202.

(42) Quarti, C.; Marchal, N.; Beljonne, D. Tuning the Optoelectronic Properties of Two-Dimensional Hybrid Perovskite Semiconductors with Alkyl Chain Spacers. *J. Phys. Chem. Lett.* **2018**, *9* (12), 3416–3424. https://doi.org/10.1021/acs.jpclett.8b01309.

(43) Pedesseau, L.; Sapori, D.; Traore, B.; Robles, R.; Fang, H.-H.; Loi, M. A.; Tsai, H.; Nie, W.; Blancon, J.-C.; Neukirch, A.; Tretiak, S.; Mohite, A. D.; Katan, C.; Even, J.; Kepenekian, M. Advances and Promises of Layered Halide Hybrid Perovskite Semiconductors. *ACS Nano* **2016**, *10* (11), 9776–9786. https://doi.org/10.1021/acsnano.6b05944.

(44) Dyksik, M.; Duim, H.; Zhu, X.; Yang, Z.; Gen, M.; Kohama, Y.; Adjokatse, S.; Maude, D. K.; Loi, M. A.; Egger, D. A.; Baranowski, M.; Plochocka, P. Broad Tunability of Carrier Effective Masses in Two-Dimensional Halide Perovskites. *ACS Energy Lett.* **2020**, *5* (11), 3609–3616. https://doi.org/10.1021/acsenergylett.0c01758.

(45) Quarti, C.; Katan, C.; Even, J. Physical Properties of Bulk, Defective, 2D and 0D Metal Halide Perovskite Semiconductors from a Symmetry Perspective. *J. Phys. Mater.* **2020**, *3* (4), 042001. https://doi.org/10.1088/2515-7639/aba6f6.

(46) Umebayashi, T.; Asai, K.; Kondo, T.; Nakao, A. Electronic Structures of Lead Iodide Based Low-Dimensional Crystals. *Phys. Rev. B* **2003**, *67* (15), 155405. https://doi.org/10.1103/PhysRevB.67.155405.

(47) Umari, P.; Mosconi, E.; De Angelis, F. Relativistic GW Calculations on $CH_3NH_3PbI_3$ and $CH_3NH_3SnI_3$ Perovskites for Solar Cell Applications. *Sci Rep* **2014**, *4* (1), 4467. https://doi.org/10.1038/srep04467.

(48) Sapori, D.; Kepenekian, M.; Pedesseau, L.; Katan, C.; Even, J. Quantum Confinement and Dielectric Profiles of Colloidal Nanoplatelets of Halide Inorganic and Hybrid Organic–Inorganic Perovskites. *Nanoscale* **2016**, *8* (12), 6369–6378. https://doi.org/10.1039/C5NR07175E.

(49) Giorgi, G.; Yamashita, K.; Palummo, M. Nature of the Electronic and Optical Excitations of Ruddlesden–Popper Hybrid Organic–Inorganic Perovskites: The Role of the Many-Body Interactions. *J. Phys. Chem. Lett.* **2018**, *9* (19), 5891–5896. https://doi.org/10.1021/acs.jpclett.8b02653.

(50) Palummo, M.; Postorino, S.; Borghesi, C.; Giorgi, G. Strong Out-of-Plane Excitons in 2D Hybrid Halide Double Perovskites. *Appl. Phys. Lett.* **2021**, *119* (5), 051103. https://doi.org/10.1063/5.0059441.

(51) Filip, M. R.; Qiu, D. Y.; Del Ben, M.; Neaton, J. B. Screening of Excitons by Organic Cations in Quasi-Two-Dimensional Organic–Inorganic Lead-Halide Perovskites. *Nano Lett.* **2022**, *22* (12), 4870–4878. https://doi.org/10.1021/acs.nanolett.2c01306.

(52) Biega, R.-I.; Filip, M. R.; Leppert, L.; Neaton, J. B. Chemically Localized Resonant Excitons in Silver–Pnictogen Halide Double Perovskites. *J. Phys. Chem. Lett.* **2021**, *12* (8), 2057–2063. https://doi.org/10.1021/acs.jpclett.0c03579.

(53) Leveillee, J.; Katan, C.; Zhou, L.; Mohite, A. D.; Even, J.; Tretiak, S.; Schleife, A.; Neukirch, A. J. Influence of π-Conjugated Cations and Halogen Substitution on the Optoelectronic and Excitonic Properties of Layered Hybrid Perovskites. *Phys. Rev. Materials* **2018**, *2* (10), 105406. https://doi.org/10.1103/PhysRevMaterials.2.105406.

(54) Quarti, C.; Giorgi, G.; Katan, C.; Even, J.; Palummo, M. Exciton Ground State Fine Structure and Excited States Landscape in Layered Halide Perovskites from Combined BSE Simulations and Symmetry Analysis. *Advanced Optical Materials n/a* (n/a), 2202801. https://doi.org/10.1002/adom.202202801.

TOC GRAPHIC

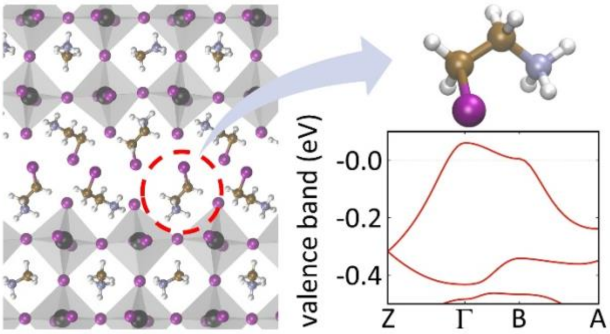

Halide containing short organic monocations in n=1-4 2D multilayered halide perovskite thin films and crystals

SUPPORTING INFORMATION

Alla Skorokhod,[a] Claudio Quarti,*[b-c] Alexandre Abhervé,[a] Magali Allain,[a] Jacky Even,[d]
Claudine Katan,[b] Nicolas Mercier*[a]

[a] MOLTECH ANJOU, UMR-CNRS 6200, Université d'Angers, 2 Bd Lavoisier, 49045 Angers, France
[b] Univ Rennes, ENSCR, INSA Rennes, CNRS, ISCR (Institut des Sciences Chimiques de Rennes) – UMR 6226, F-35000 Rennes, France
[c] Laboratory for Chemistry of Novel Materials, Materials Research Institute, University of Mons, Place du Parc 20, 7000-Mons, Belgium
[d] Univ Rennes, INSA Rennes, CNRS, Institut FOTON - UMR 6082, F-35000 Rennes, France
Corresponding authors: claudio.quarti@umons.ac.be
nicolas.mercier@univ-angers.fr

Table of contents

1. Details for the synthesis of $(I\text{-}C_2H_4\text{-}NH_3)_2(CH_3NH_3)_{n-1}[Pb_nI_{3n+1}]$ crystal powders

Table S1. Solutions for preparation the crystals of $(IEA)_2MA_{n-1}Pb_nI_{3n+1}$ ($I\text{-}EA=I\text{-}C_2H_4\text{-}NH_3$ and $MA=CH_3NH_3$).

	$Br\text{-}C_2H_4\text{-}NH_2•HBr$	**$CH_3NH_2•HI$**	**PbI_2**	**HI**
n=1 **$(I\text{-}C_2H_4NH_3)_2[PbI_4]$**	**205 mg**	**-**	**230.5**	**2 ml**
	1 mmol		**0.5 mmol**	
	2		1	
n=2 **$(I\text{-}C_2H_4\text{-}NH_3)_2(CH_3NH_3)[Pb_2I_7]$**	**102.5 mg**	**39.8 mg**	**230.5 mg**	**2 ml**
	0.5 mmol	**0.25 mmol**	**0.5 mmol**	
	2	1	2	
n=3 **$(I\text{-}C_2H_4\text{-}NH_3)_2(CH_3NH_3)_2[Pb_3I_{10}]$**	**69.7 mg**	**54.1 mg**	**235.1 mg**	**2 ml**
	0.34 mmol	**0.34 mmol**	**0.51 mmol**	
	2	2	3	
n=4 **$(I\text{-}C_2H_4\text{-}NH_3)_2(CH_3NH_3)_3[Pb_4I_{13}]$**	**51.2 mg**	**59.6 mg**	**230.5 mg**	**2 ml**
	0.25 mmol	**0.375 mmol**	**0.5 mmol**	
	2	3	4	

2. Details for the synthesis of $(I\text{-}C_2H_4\text{-}NH_3)_2(CH_3NH_3)_{n-1}[Pb_nI_{3n+1}]$ thin films

Table S2. Solutions for preparation the thin films of $(IEA)_2MA_{n-1}Pb_nI_{3n+1}$ ($I\text{-}EA=I\text{-}C_2H_4\text{-}NH_3$ and $MA=CH_3NH_3$).

Solutions for preparation the thin films				
	$(I\text{-}C_2H_4NH_3)_2[PbI_4]$	**CH_3NH_3I**	**PbI_2**	**DMSO**
n=1 **$(I\text{-}C_2H_4NH_3)_2[PbI_4]$**	**254 mg**	**-**	**-**	**0.2 ml**
	0.24 mmol			
n=2 **$(I\text{-}C_2H_4NH_3)_2(CH_3NH_3)[Pb_2I_7]$**	**127 mg**	**19 mg**	**55 mg**	**0.2 ml**
	0.12 mmol	**0.12 mmol**	**0.12 mmol**	
n=3 **$(I\text{-}C_2H_4NH_3)_2(CH_3NH_3)_2[Pb_3I_{10}]$**	**84.6 mg**	**25.4mg**	**73.8 mg**	**0.2 ml**
	0.08 mmol	**0.16 mmol**	**0.16 mmol**	
n=4 **$(I\text{-}C_2H_4NH_3)_2(CH_3NH_3)_3[Pb_4I_{13}]$**	**63.5 mg**	**28.6 mg**	**83**	**0.2 ml**
	0.06 mmol	**0.18 mmol**	**0.18 mmol**	

3. Powder XRD characterization

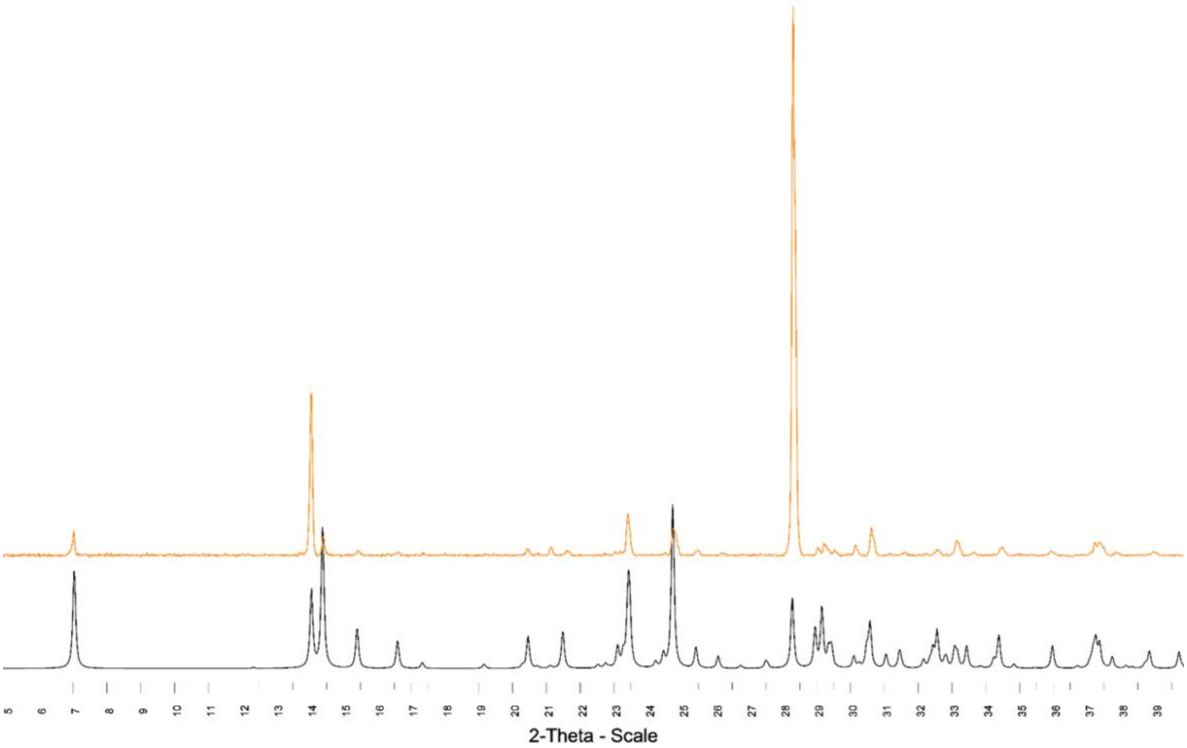

Figure S1. PXRD patterns of n=1, (I-EA)$_2$PbI$_4$: simulated (black line) and experimental (orange line).

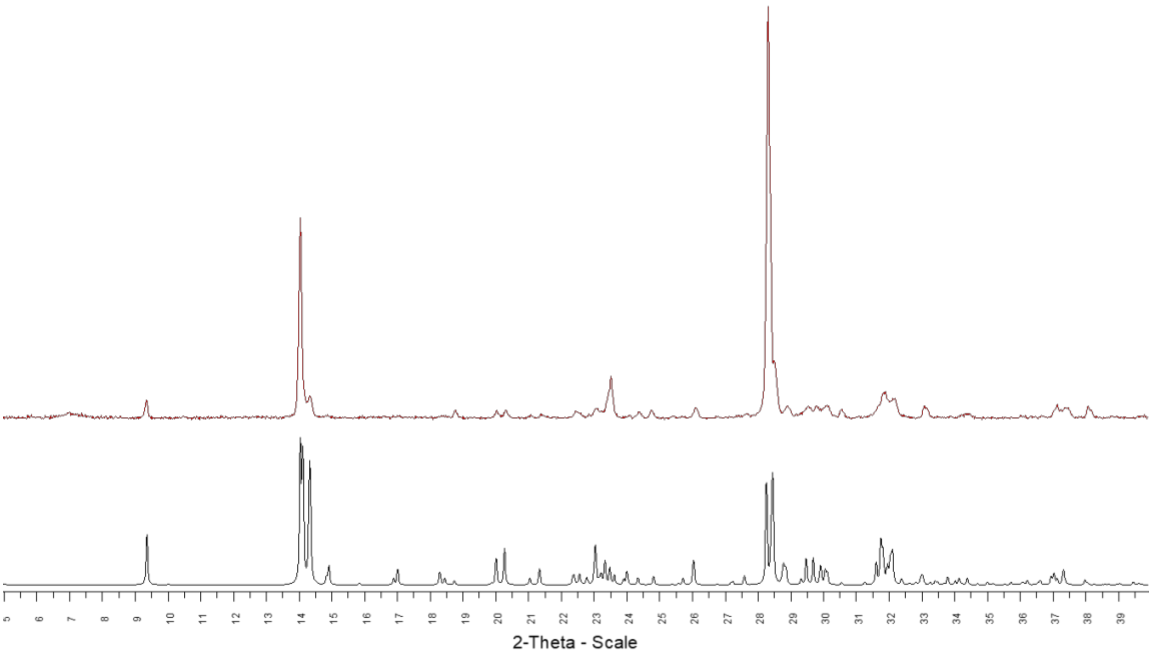

Figure S2. Room temperature PXRD patterns of n=2, (I-EA)$_2$MAPb$_2$I$_7$: simulated (black line) and experimental (red line).

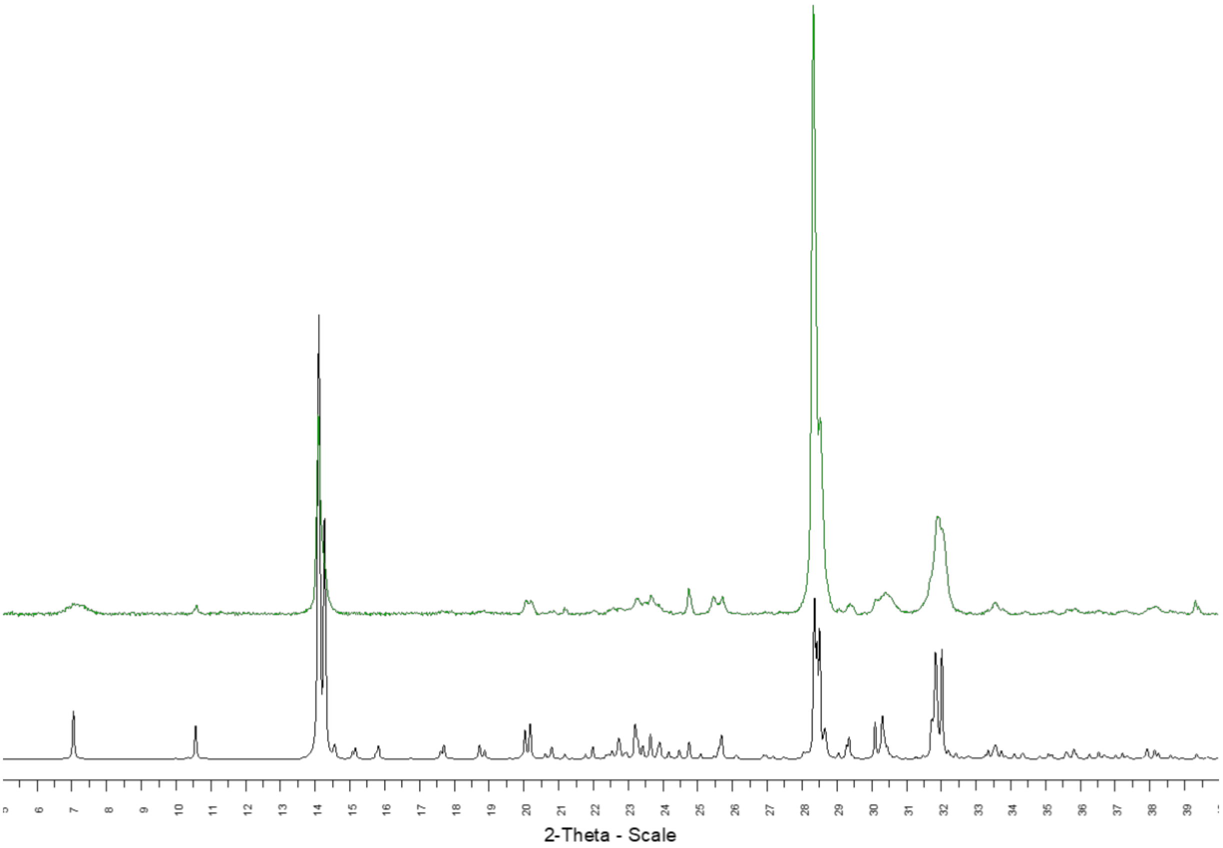

Figure S3. PXRD patterns of n=3, $(I\text{-}EA)_2MA_2Pb_3I_{10}$: simulated (black line) and experimental (green line).

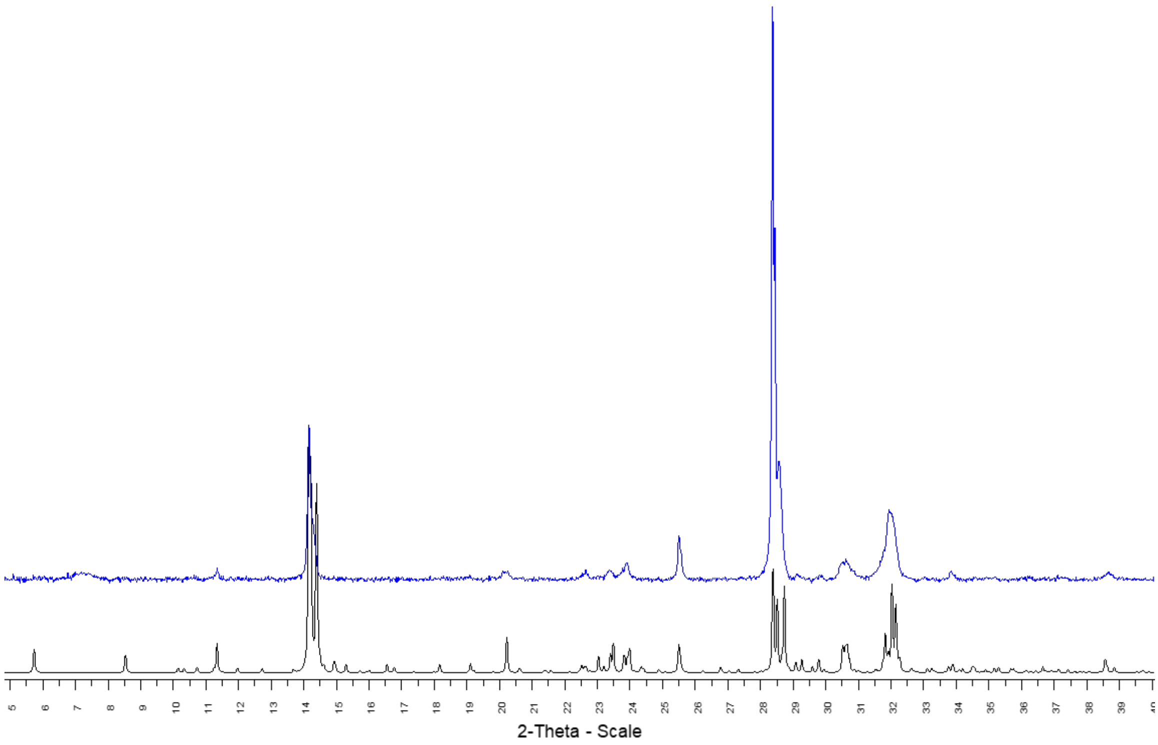

Figure S4. PXRD patterns of n=4, $(\text{I-EA})_2\text{MA}_3\text{Pb}_4\text{I}_{13}$: simulated (black line) and experimental (blue line).

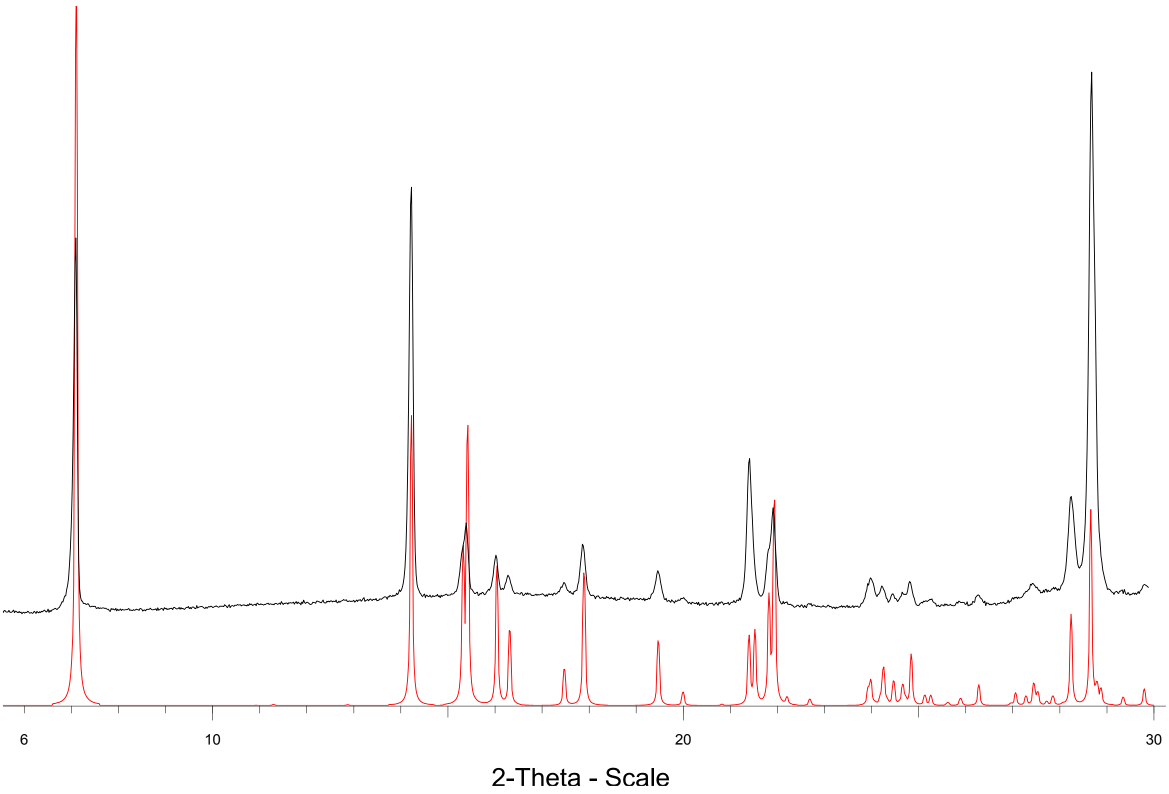

Figure S5. PXRD patterns of n=1, $(Br\text{-}EA)_2PbBr_4$ ($Br\text{-}EA=Br(CH_2)_2NH_3$): simulated (in the room temperature unit cell: a= 8.16 Å, b= 8.25 Å, c= 25.09 Å, α= 90°, β= 97.0°, γ= 90° -red line-) and experimental (black line).

4. ^{1}H NMR characterization in solution

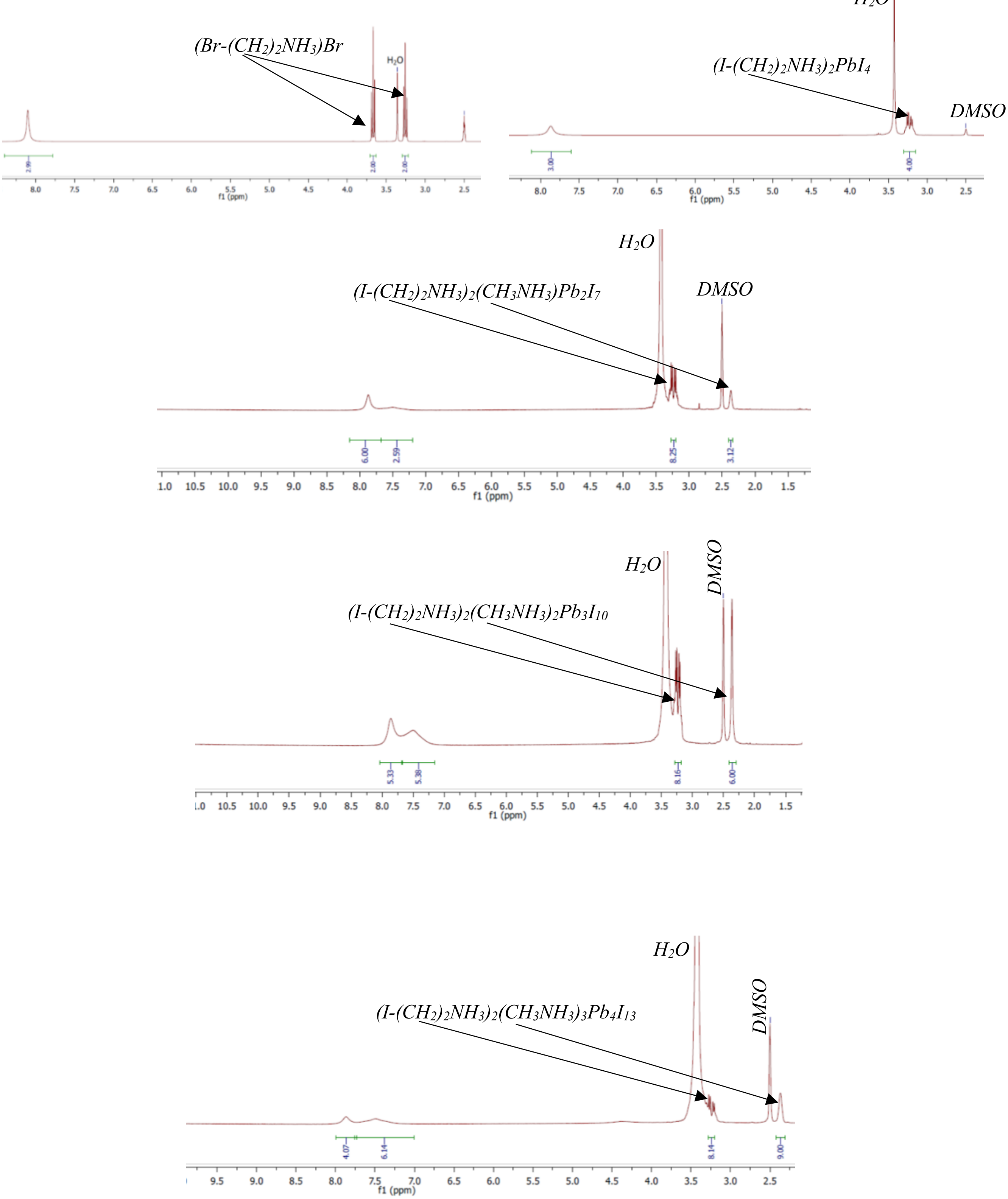

Figure S6. ^{1}H NMR of crystallized powders of (Br-$(CH_2)_2NH_3$)Br and (I-EA)$_2$MA$_{n-1}$Pb$_n$I$_{3n+1}$ (n= 1, 4), showing that "(I-$(CH_2)_2NH_3$)/(CH_3NH_3)" ratio of 1.98 (n= 2), 1.02 (n= 3) and 0.678 (n= 4) are close to the expected one (2 (n= 2), 1 (n= 3) and 0.667 (n= 4).

5. Resolved crystal structures

Table S3. Crystal data and structure refinement for n=1, $(\text{I-EA})_2\text{PbI}_4$ at T = 120K.

Empirical formula	C4 H14 I6 N2 Pb
Formula weight	1058.77
Temperature	120 K
Wavelength	1.54184 A
Crystal system, space group	Monoclinic, P 21/c
Unit cell dimensions	a = 12.5049(4) A alpha = 90 deg.
	b = 8.7414(3) A beta = 97.880(3) deg.
	c = 8.6297(3) A gamma = 90 deg.
Volume	934.41(5) A^3
Z, Calculated density	2, 3.763 Mg/m^3
Absorption coefficient	95.186 mm^-1
F(000)	904
Crystal size	0.183 x 0.142 x 0.042 mm
Theta range for data collection	3.568 to 71.875 deg.
Limiting indices	-15<=h<=14, -10<=k<=9, -10<=l<=10
Reflections collected / unique	3466 / 1791 [R(int) = 0.0295]
Completeness to theta = 70.000	99.0 %
Refinement method	Full-matrix least-squares on F^2
Data / restraints / parameters	1791 / 0 / 62
Goodness-of-fit on F^2	1.111
Final R indices [I>2sigma(I)]	R1 = 0.0485, wR2 = 0.1247
R indices (all data)	R1 = 0.0491, wR2 = 0.1255
Largest diff. peak and hole	3.001 and -5.494 e.A^-3

Table S4. Crystal data and structure refinement for n=2, (I-EA)$_2$MAPb$_2$I$_7$ at T = 150K.

Empirical formula	C5 H20 I9 N3 Pb2 or Pb2 I7, 2(C2 H7 I N), C H6 N
Formula weight	1678.72
Temperature	150.0(3) K
Wavelength	1.54184 A
Crystal system, space group	Triclinic, P -1
Unit cell dimensions	a = 8.8125(4) A alpha = 107.560(5) deg.
	b = 17.4198(10) A beta = 96.005(4) deg.
	c = 19.6320(11) A gamma = 90.363(4) deg.
Volume	2855.3(3) A^3
Z, Calculated density	4, 3.905 Mg/m^3
Absorption coefficient	99.029 mm^-1
F(000)	2848
Crystal size	0.12 x 0.10 x 0.025 mm – red plate
Theta range for data collection	2.663 to 72.476 deg.
Limiting indices	-10<=h<=5, -15<=k<=20, -15<=l<=24
Reflections collected / unique	8937 / 6491 [R(int) = 0.0579]
Completeness to theta = 67.684	60.8 %
Absorption correction	Semi-empirical from equivalents
Max. and min. transmission	1.00000 and 0.21427
Refinement method	Full-matrix least-squares on F^2
Data / restraints / parameters	6491 / 56 / 345
Goodness-of-fit on F^2	1.050
Final R indices [I>2sigma(I)]	R1 = 0.0699, wR2 = 0.1810 [5018 Fo]
R indices (all data)	R1 = 0.0844, wR2 = 0.2010
Largest diff. peak and hole	2.946 and -3.674 e.A^-3

Table S5. Crystal data and structure refinement for n=2, (I-EA)$_2$MAPb$_2$I$_7$ at T = 293K.

Empirical formula	C5 H20 I9 N3 Pb2
Formula weight	1678.72
Temperature	293(2) K
Wavelength	0.71073 A
Crystal system, space group	Triclinic, P -1
Unit cell dimensions	a = 8.8172(8) A alpha = 82.686(6) deg.
	b = 8.9178(4) A beta = 83.401(7) deg.
	c = 19.213(2) A gamma = 90.072(5) deg.
Volume	1488.3(2) A^3
Z, Calculated density	2, 3.746 Mg/m^3
Absorption coefficient	20.627 mm^-1
F(000)	1424
Crystal size	0.284 x 0.198 x 0.031 mm - red plate
Theta range for data collection	2.303 to 27.499 deg.
Limiting indices	-11<=h<=11, -11<=k<=11, -24<=l<=24
Reflections collected / unique	27410 / 6778 [R(int) = 0.1062]
Completeness to theta = 27.499	99.0 %
Absorption correction	Semi-empirical from equivalents
Max. and min. transmission	0.528 and 0.225
Refinement method	Full-matrix least-squares on F^2
Data / restraints / parameters	6778 / 49 / 175
Goodness-of-fit on F^2	1.030
Final R indices [I>2sigma(I)]	R1 = 0.0908, wR2 = 0.2057 [3134 Fo]
R indices (all data)	R1 = 0.2126, wR2 = 0.2394
Largest diff. peak and hole	2.892 and -2.096 e.A^-3

Table S6. Crystal data and structure refinement for n=3, $(I\text{-}EA)_2MA_2Pb_3I_{10}$ at T = 150K.

Empirical formula	C6 H26 I12 N4 Pb3
Formula weight	1149.34
Temperature	150.0(2) K
Wavelength	1.54184 A
Crystal system, space group	Monoclinic, P 21/c
Unit cell dimensions	a = 25.1387(14) A alpha = 90 deg.
	b = 8.8768(5) A beta = 94.346(6) deg.
	c = 8.6144(5) A gamma = 90 deg.
Volume	1916.79(19) A^3
Z, Calculated density	2, 3.983 Mg/m^3
Absorption coefficient	101.112 mm^-1
F(000)	1944
Crystal size	0.105 x 0.088 x 0.024 mm
Theta range for data collection	3.527 to 72.912 deg.
Limiting indices	-27<=h<=31, -9<=k<=10, -8<=l<=10
Reflections collected / unique	7288 / 3622 [R(int) = 0.0562]
Completeness to theta = 70.000	96.7 %
Refinement method	Full-matrix least-squares on F^2
Data / restraints / parameters	3622 / 0 / 118
Goodness-of-fit on F^2	1.205
Final R indices [I>2sigma(I)]	R1 = 0.0780, wR2 = 0.2122
R indices (all data)	R1 = 0.0819, wR2 = 0.2149
Largest diff. peak and hole	5.221 and -3.237 e.A^-3

Table S7. Crystal data and structure refinement for n=4, $(I\text{-}EA)_2MA_3Pb_4I_{13}$ at T = 150K

Empirical formula	C7 H32 I15 N5 Pb4
Formula weight	2918.63
Temperature	150.0(1) K
Wavelength	1.54184 A
Crystal system, space group	Triclinic, P -1
Unit cell dimensions	a = 8.7713(3) A alpha = 85.631(3) deg.
	b = 8.8359(3) A beta = 85.116(3) deg.
	c = 31.4225(11) A gamma = 89.997(3) deg.
Volume	2419.37(14) A^3
Z, Calculated density	2, 4.006 Mg/m^3
Absorption coefficient	101.780 mm^-1
F(000)	2464
Crystal size	0.087 x 0.080 x 0.027 mm
Theta range for data collection	2.831 to 76.218 deg.
Limiting indices	-11<=h<=10, -9<=k<=7, -38<=l<=39
Reflections collected / unique	14099 / 8079 [R(int) = 0.0323]
Completeness to theta = 70.000	82.7 %
Absorption correction	Gaussian
Max. and min. transmission	0.570 and 0.165
Refinement method	Full-matrix least-squares on F^2
Data / restraints / parameters	8079 / 19 / 317
Goodness-of-fit on F^2	1.075
Final R indices [I>2sigma(I)]	R1 = 0.0622, wR2 = 0.1639 [7261 Fo]
R indices (all data)	R1 = 0.0669, wR2 = 0.1688
Largest diff. peak and hole	3.393 and -5.993 e.A^-3

Table S8. Crystal data and structure refinement for n=1, $(Br\text{-}EA)_2PbBr_4$ at T = 150K.

Empirical formula	C4 H14 Br6 N2 Pb ou Pb Br4, 2(C2 H7 Br N)
Formula weight	776.82
Temperature	150.0(1) K
Wavelength	1.54184 A
Crystal system, space group	Triclinic, P -1
Unit cell dimensions	a = 8.2313(4) A alpha = 66.190(4) deg.
	b = 13.6632(6) A beta = 81.310(3) deg.
	c = 15.8766(6) A gamma = 80.955(4) deg.
Volume	1605.69(13) A^3
Z, Calculated density	4, 3.213 Mg/m^3
Absorption coefficient	37.695 mm^-1
F(000)	1376
Crystal size	0.188 x 0.073 x 0.032 mm – colorless plate
Theta range for data collection	3.057 to 72.248 deg.
Limiting indices	-9<=h<=8, -16<=k<=16, -18<=l<=19
Reflections collected / unique	11994 / 6034 [R(int) = 0.0489]
Completeness to theta = 69.000	98.0 %
Absorption correction	Gaussian
Max. and min. transmission	0.416 and 0.045
Refinement method	Full-matrix least-squares on F^2
Data / restraints / parameters	6034 / 0 / 242
Goodness-of-fit on F^2	1.061
Final R indices [I>2sigma(I)]	R1 = 0.0580, wR2 = 0.1649 [5612 Fo]
R indices (all data)	R1 = 0.0599, wR2 = 0.1684
Largest diff. peak and hole	4.789 and -4.549 e.A^-3

6. Computational details

Band structures and diagonal components of the electron/hole effective mass tensor. These are computed employing plane-wave/pseudopotential, periodic DFT calculations, as implemented in the Quantum-Espresso package.[1] They employed 25 and 200 Ry cutoff for the plane-wave expansion of the single particle states and electronic density, respectively, along with ultrasoft pseudopotentials.[2] The present approach was shown to provide a good trade-off between accuracy and computational cost.[3] These calculations are performed within GGA approximation, adopting the PBE exchange-correlation functional.[4] Due to the presence of heavy lead atoms, we explicitly accounted for Spin-Orbit-Coupling (SOC) interaction.[5,6] Lattice parameters and atomic positions of the inorganic frame are kept frozen, to preserve the structural details associated to the different phases of n=1 and n=2 compounds (vide-infra). Atomic positions of the organic moieties have been relaxed, accounting for dispersive interactions via the Grimme DFT-D2 method.[7] From the computed band dispersions, the diagonal component of the effective mass tensor was estimated by routinely fitting the curvature of the top valence and bottom conduction band, for hole and electrons, respectively.

High-frequency dielectric profiles. These are calculated using atomic-centered, periodic DFT calculations, using the SIESTA code.[8] Core electrons are described with Troullier-Martins pseudopotentials,[9] while the valence wavefunction is developed over a double-zeta polarized basis set of finite-range numerical pseudoatomic orbitals. The procedure for obtaining dielectric profile is based on the definition of the dielectric constant as related to the induced polarization (p_{ind})in the material, in response to an external electric field.[10,11] Therefore, calculations on slab models are performed with and without an external field oriented along the plane stacking variation (E_{EXT} set here to 0.01 V/Å) and the variation of the electronic density profile along the same direction ($\delta\rho(z)$) is hence determined. The induced polarization is then obtained from the integration of:

$$\frac{dp_{ind}(z)}{dz} = -\delta\rho(z)$$

This leads to the calculation of the dielectric constant as:

$$\varepsilon_\infty(z) = \frac{\varepsilon_\infty E_{EXT}}{\varepsilon_\infty E_{EXT} - p_{ind}(z)}$$

Both plane-waves/pseudopotentials (Quantum-Espresso) and atomic based (SIESTA) DFT calculations employed regular sampling of the Brillouin zone in the Monkhorst-Pack scheme.[12] Different sampling have been used for the various components as listed in Table S9, so to reflect the variations in the direct lattice parameters.

Table S9. Automatic sampling of the first Brillouin Zone (BZ) adopted in the periodic DFT simulations of the reported (X-EA)$_2$MA$_{n-1}$Pb$_n$I$_{3n+1}$ (X=Cl, Br, I) compounds and (Br-EA)$_2$PbBr$_4$.

Compound	**T (K)**	**Space group**	**a**	**b**	**c**	**BZ Sampling**
(Cl-EA)$_2$PbI$_4$*	293	Pbnm	6.4703	12.8397	20.7972	6 x 3 x 4
(Br-EA)$_2$PbI$_4$*	293	Pbnm	6.4824	12.9046	21.1412	6 x 3 x 4
(I-EA)$_2$PbI$_4$*	293	P2$_1$/a	8.7531	8.7471	12.7202	4 x 4 x 2
	120	P2$_1$/c	12.5049	8.7414	8.6297	2 x 4 x 4
(I-EA)$_2$MA$_1$Pb$_2$I$_7$	293	P-1	8.8172	8.9178	19.2132	4 x 4 x 2
	150	P-1	8.8125	17.4198	19.6320	4 x 2 x 2
(I-EA)$_2$MA$_2$Pb$_3$I$_{10}$	150	P2$_1$/c	25.1891	8.8768	8.6144	4 x 4 x 2
(I-EA)$_2$MA$_2$Pb$_3$I$_{10}$	150	P-1	8.7713	8.8359	31.4221	4 x 4 x 2
(Br-EA)$_2$PbBr$_4$	150	P-1	8.2313	13.6632	15.8766	4 x 3 x 3

* Crystal structures from Chem. Mater., 19, 600 (2007)

Semi-empirical solution of the Bethe-Salpeter Equations (BSE). These are obtained via a 3D momentum space representation for the polarization function P_{eh} that accounts for statically screened electron-hole potential interaction V_s.

$$P_{eh}(\boldsymbol{k}_e,\boldsymbol{k}_h,E) = P_{eh}^0(\boldsymbol{k}_e,\boldsymbol{k}_h,E) - \sum_{\boldsymbol{k}}\sum_{\boldsymbol{k}\prime} P_{eh}^0(\boldsymbol{k}_e,\boldsymbol{k},E)V_s(|\boldsymbol{k}-\boldsymbol{k}'|)P_{eh}^0(\boldsymbol{k}',\boldsymbol{k}_h,E)$$

where $\boldsymbol{k}_e$($\boldsymbol{k}_h$) is the electron(hole) wavevector in momentum space and E is the energy.

The definition of the bzero-order polarization function P_{eh}^0 is based here on the effective-mass approximation:

$$P_{eh}^0(\boldsymbol{k}_e,\boldsymbol{k}_h,E) = \frac{1}{E - E_g - \frac{\hbar^2|\boldsymbol{k}_e|^2}{2\mu} + i\Gamma}\delta_{\boldsymbol{k}_e,\boldsymbol{k}_h}$$

Here, E_g is the free charge electronic band gap, μ is the effective mass of the exciton and Γ is a broadening factor.

The potential function V_s is expressed in the Fourier space, as follows:

$$V_s(q_t) = \frac{-e^2}{2\varepsilon_w q_t}\int_{-\frac{d}{2}}^{\frac{d}{2}}\int_{-\frac{d}{2}}^{\frac{d}{2}} \rho_e(z_e)\rho_h(z_h)\left[e^{-q_t|z_e-z_h|} + \Delta\chi\left(e^{-q_t|z_e+z_h-d|} + e^{-q_t|z_e+z_h\}d|}\right)\right]$$

$$+\Delta\chi^2\left(e^{-q_t|z_e-z_h-2d|} + e^{-q_t|z_H+z_e-2d|}\right)dz_e dz_h$$

Where:

- $q_t = |\boldsymbol{k}_e - \boldsymbol{k}_h|$ being the difference of electron and hole transverse (in-plane) wavevectors.
- ρ_e and ρ_h are the electron and hole probability density profiles along the plane stacking direction
- $\Delta = (1 - \chi^2 e^{-2q_t d})^{-1}$ representing
- $\chi = \frac{\varepsilon_w - \varepsilon_b}{\varepsilon_w + \varepsilon_b}$

More details about the derivation and implementation of this formalism can be found in Ref.[13]

7. Structural analysis

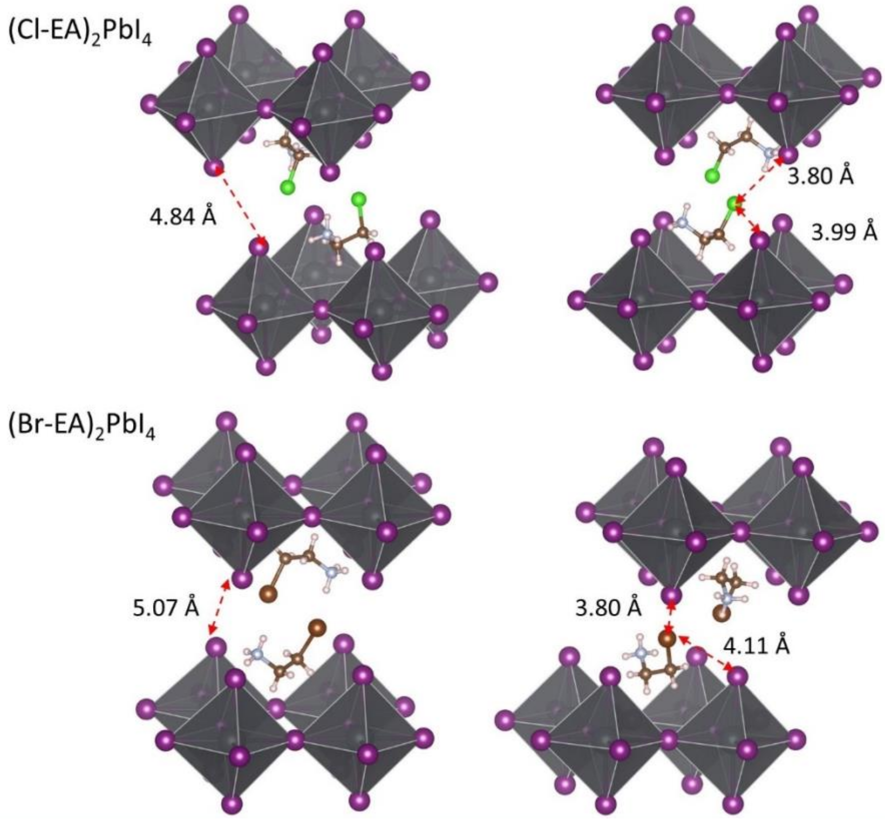

Figure S7. Structural details associated to n=1 (Cl-EA)$_2$PbI$_4$ and (Br-EA)$_2$PbI$_4$ layered halide perovskites. Interlayer distance (left) and shortest distance between the halide from the spacer and the apical iodines from the inorganic frame (right) are indicated.

Table S10. Structural details and band gap (E_g) of newly synthesized 2D layered halide perovskites. Averaged and standard deviation of the lead-halide distance (Pb-X) within the inorganic frame, lead-halide-lead valence bond angle (Pb-I-Pb), averaged Baur elongation parameter (D) and angular octahedral distortion (σ_{oct}).

compound	**T (K)**	**Pb-X (Å)**		**Pb-I-Pb (deg)**		**D**	**σ_{oct} (deg^2)**	**E_g (eV)**
		average	**st. dev**	**average**	**st. dev.**			
(Cl-EA)$_2$PbI$_4^*$	293	3.22	0.03	177.37	0.25	0.030	8.68	1.01
(Br-EA)$_2$PbI$_4^*$	293	3.22	0.04	177.23	0.11	0.036	5.56	1.03
(I-EA)$_2$PbI$_4^*$	293	3.21	0.02	147.38	N.A.	0.020	2.74	1.40
	120	3.19	0.02	146.83	N.A.	0.023	4.46	1.38
(I-EA)$_2$MA$_1$Pb$_2$I$_7$	293	3.18	0.04	161.86	0.68	0.030	3.51	0.96
	150	3.17	0.05	157.38	1.27	0.042	5.43	1.06
(I-EA)$_2$MA$_2$Pb$_3$I$_{10}$	150	3.18	0.05	156.14	3.53	0.030	17.43	0.95
(I-EA)$_2$MA$_2$Pb$_4$I$_{13}$	150	3.18	0.05	162.44	1.00	0.037	6.12	0.79
(Br-EA)$_2$PbBr$_4$	150	2.99	0.04	148.33	2.12	0.033	6.31	1.79

8. Tauc plot analysis

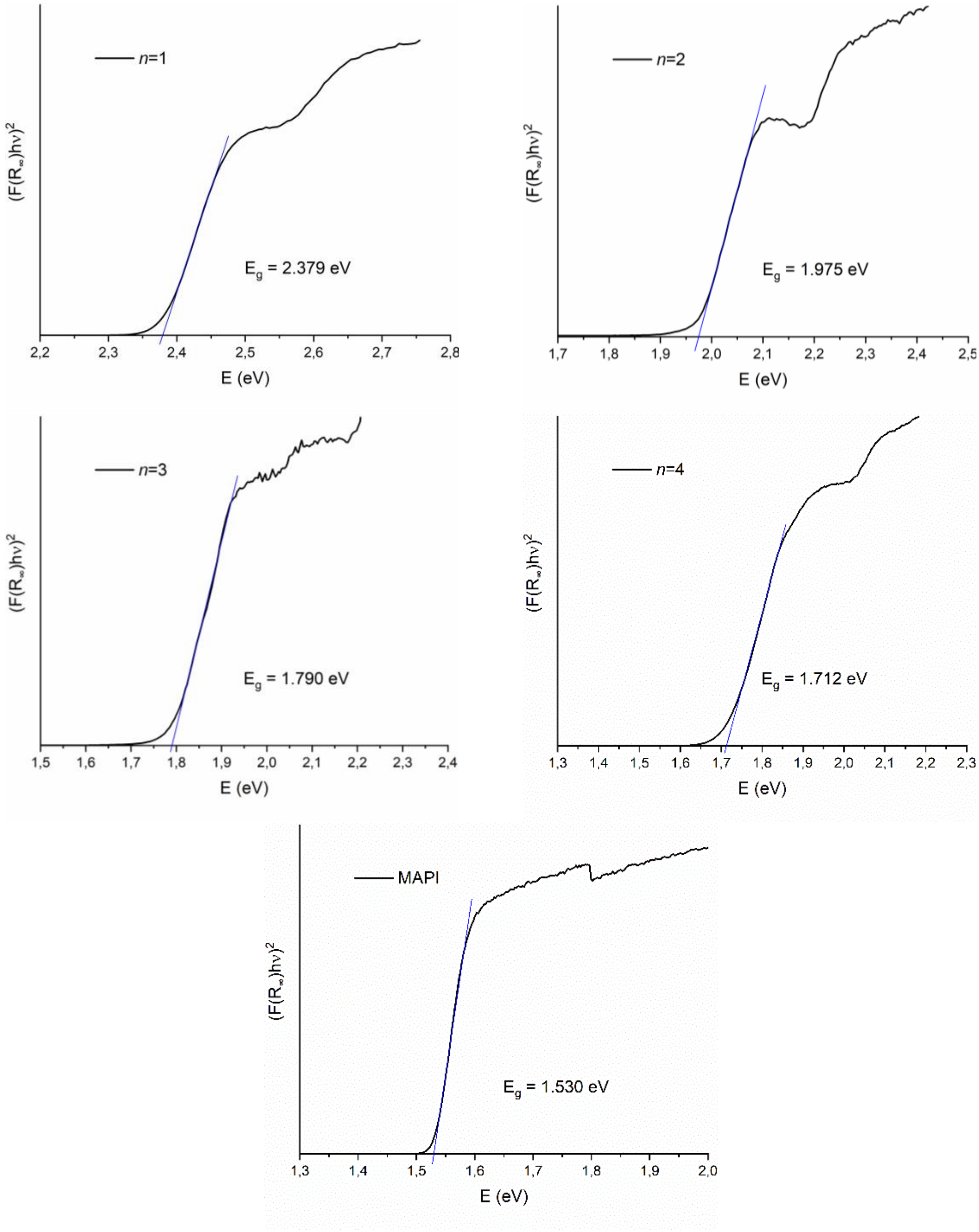

Figure S8. TAUC plot for $(I\text{-}EA)_2MA_{n-1}Pb_nI_{3n+1}$ (n= 1-4), calculated from absorbance spectra of crystallized powders (see Figure 3). TAUC plot for MAPbI is also reported, for reference.

9. Optical absorption and morphology of thin-films

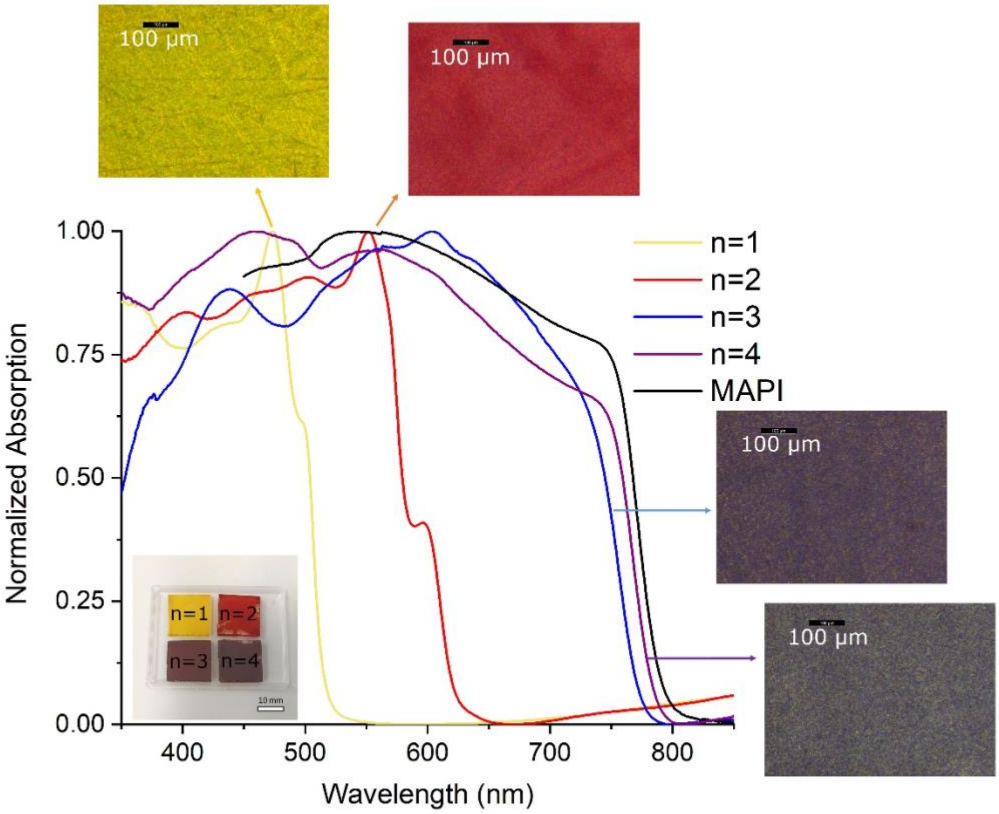

Figure S9. UV-vis absorption of thin films of multi-n (I-EA)$_2$MA$_{n-1}$Pb$_n$I$_{3n+1}$ (n= 1-4) samples. The absorption spectrum of $CH_3NH_3PbI_3$ (MAPI) is also reported, as reference. Pictures of the thin films are reported as well, to highlight the good morphologic and color homogeneity of the samples and the gradual change of color with increasing perovskite layer thickness n.

10. Comparison of the dielectric profile for Bromine and Iodine -based compounds

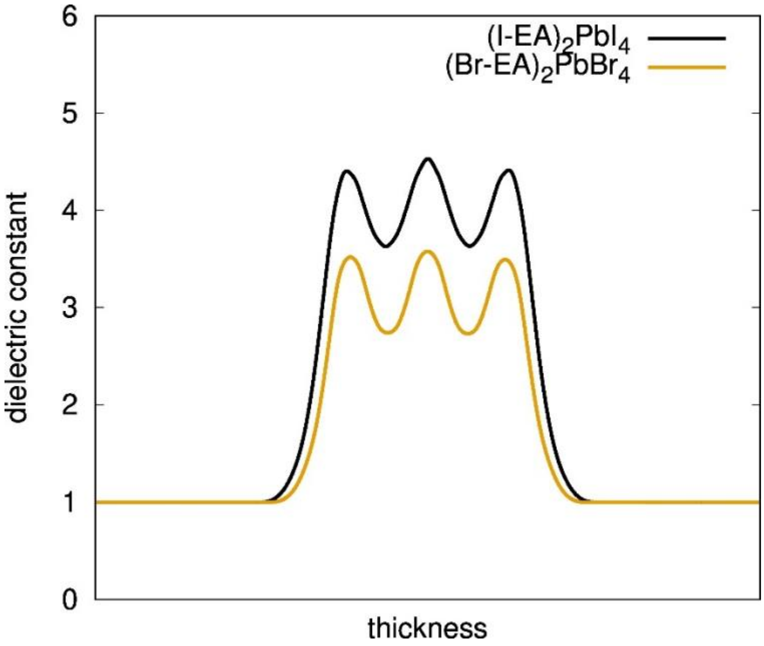

Figure S10. DFT computed dielectric profile for n=1 $(I\text{-}EA)_2PbI_4$, and $(Br\text{-}EA)_2PbBr_4$ compounds.

11. References

(1) Giannozzi, P.; Baroni, S.; Bonini, N.; Calandra, M.; Car, R.; Cavazzoni, C.; Ceresoli, D.; Chiarotti, G. L.; Cococcioni, M.; Dabo, I.; Corso, A. D.; Gironcoli, S. de; Fabris, S.; Fratesi, G.; Gebauer, R.; Gerstmann, U.; Gougoussis, C.; Kokalj, A.; Lazzeri, M.; Martin-Samos, L.; Marzari, N.; Mauri, F.; Mazzarello, R.; Paolini, S.; Pasquarello, A.; Paulatto, L.; Sbraccia, C.; Scandolo, S.; Sclauzero, G.; Seitsonen, A. P.; Smogunov, A.; Umari, P.; Wentzcovitch, R. M. QUANTUM ESPRESSO: A Modular and Open-Source Software Project for Quantum Simulations of Materials. *J. Phys.: Condens. Matter* 2009, *21* (39), 395502. https://doi.org/10.1088/0953-8984/21/39/395502.

(2) Vanderbilt, D. Soft Self-Consistent Pseudopotentials in a Generalized Eigenvalue Formalism. *Phys. Rev. B* 1990, *41* (11), 7892–7895. https://doi.org/10.1103/PhysRevB.41.7892.

(3) Quarti, C.; Mosconi, E.; De Angelis, F. Interplay of Orientational Order and Electronic Structure in Methylammonium Lead Iodide: Implications for Solar Cell Operation. *Chem. Mater.* 2014, *26* (22), 6557–6569. https://doi.org/10.1021/cm5032046.

(4) Perdew, J. P.; Burke, K.; Ernzerhof, M. Generalized Gradient Approximation Made Simple. *Phys. Rev. Lett.* 1996, *77* (18), 3865–3868. https://doi.org/10.1103/PhysRevLett.77.3865.

(5) Even, J.; Pedesseau, L.; Jancu, J.-M.; Katan, C. Importance of Spin–Orbit Coupling in Hybrid Organic/Inorganic Perovskites for Photovoltaic Applications. *J. Phys. Chem. Lett.* 2013, *4* (17), 2999–3005. https://doi.org/10.1021/jz401532q.

(6) Quarti, C.; Marchal, N.; Beljonne, D. Tuning the Optoelectronic Properties of Two-Dimensional Hybrid Perovskite Semiconductors with Alkyl Chain Spacers. *J. Phys. Chem. Lett.* 2018, *9* (12), 3416–3424. https://doi.org/10.1021/acs.jpclett.8b01309.

(7) Grimme, S. Semiempirical GGA-type density functional constructed with a long-range dispersion correction. *Journal of Computational Chemistry* 2006, *27* (15), 1787–1799. https://doi.org/10.1002/jcc.20495.

(8) Soler, J. M.; Artacho, E.; Gale, J. D.; García, A.; Junquera, J.; Ordejón, P.; Sánchez-Portal, D. The SIESTA Method Forab Initioorder-Nmaterials Simulation. *J. Phys.: Condens. Matter* 2002, *14* (11), 2745–2779. https://doi.org/10.1088/0953-8984/14/11/302.

(9) Troullier, N.; Martins, J. L. Efficient Pseudopotentials for Plane-Wave Calculations. *Phys. Rev. B* 1991, *43* (3), 1993–2006. https://doi.org/10.1103/PhysRevB.43.1993.

(10) Even, J.; Pedesseau, L.; Kepenekian, M. Electronic Surface States and Dielectric Self-Energy Profiles in Colloidal Nanoscale Platelets of CdSe. *Phys. Chem. Chem. Phys.* 2014, *16* (45), 25182–25190. https://doi.org/10.1039/C4CP03267E.

(11) Sapori, D.; Kepenekian, M.; Pedesseau, L.; Katan, C.; Even, J. Quantum Confinement and Dielectric Profiles of Colloidal Nanoplatelets of Halide Inorganic and Hybrid Organic–Inorganic Perovskites. *Nanoscale* 2016, *8* (12), 6369–6378. https://doi.org/10.1039/C5NR07175E.

(12) Monkhorst, H. J.; Pack, J. D. Special Points for Brillouin-Zone Integrations. *Phys. Rev. B* 1976, *13* (12), 5188–5192. https://doi.org/10.1103/PhysRevB.13.5188.

(13) Blancon, J.-C.; Stier, A. V.; Tsai, H.; Nie, W.; Stoumpos, C. C.; Traoré, B.; Pedesseau, L.; Kepenekian, M.; Katsutani, F.; Noe, G. T.; Kono, J.; Tretiak, S.; Crooker, S. A.; Katan, C.; Kanatzidis, M. G.; Crochet, J. J.; Even, J.; Mohite, A. D. Scaling Law for Excitons in 2D Perovskite Quantum Wells. *Nat Commun* 2018, *9* (1), 2254. https://doi.org/10.1038/s41467-018-04659-x.